# 1 Introduction

We are curious what happens to the atoms which are influenced by external forces especially by the dipole-dipole interaction. Because of the superior properties (sensitivity to eternal fields, large collision sections and etc.), Rydberg atoms are perfect objects for researching electron dynamics. We also use Magneto-Optical Trap to freeze atoms, so that during the dipole-dipole interaction period, the atoms are considered to be static. This dissertation discusses the influence of dipole-dipole interaction on electron dynamics in cold Rydberg atoms. In this dissertation, three independent experiments are presented, as well as the simulation results.

# 1.1 Rydberg Atoms and Dipole-Dipole Interaction

Rydberg atoms are atoms in which an electron is excited to a state with a high principal quantum number. Usually this number is larger than 10. They are good systems for researching atom dynamics. The details about Rydberg atoms and their properties are described in Chapter 3.

Dipole-Dipole interaction happens between two close Rydberg atoms. Such an interaction is a result of electric fields produced by external electrons and charged atom cores. Because of dipole-dipole interaction, the Rydberg atoms could not be considered as individual one but a system. The details about dipole-dipole interaction, both from classic view and quantum view, could be found in Chapter 3.

# 1.2 Atomic Units

Atomic units (au or a.u.) are commonly used in atomics research. The concept originates from the research of the ground state of hydrogen. For convenience, if we define:

$$\hbar = m_e = e = 4\pi\varepsilon_0 = 1 \tag{1.1}$$

where $\hbar$ is Planck's constant divided by $2\pi$, $m_e$ is the mass of the electron, $-e$ is the charge of the electron, and $\varepsilon_0$ is the permittivity of free space, we can get the express for different quantities in atomic units as shown in Table 1.1.

| Quantity | Value in atomic units | Value in SI units |
|---|---|---|
| Length | 1 | $5.2917721092(17)\times10^{-11}$ m |
| Energy | 1 | $4.35974417(75)\times10^{-18}$ J |
| Time | 1 | $2.418884326505(16)\times10^{-17}$ s |
| Velocity | 1 | $2.1876912633(73)\times10^{6}$ m·s$^{-1}$ |
| Force | 1 | $8.2387225(14)\times10^{-8}$ N |
| Temperature | 1 | $3.1577464(55)\times10^{5}$ K |
| Pressure | 1 | $2.9421912(19)\times10^{13}$ Pa |

| Electric field | 1 | $5.14220652(11) \times 10^{11}$ V·m$^{-1}$ |
|---|---|---|
| Electric potential | 1 | $2.721138505(60) \times 10^{1}$ V |
| Electric dipole moment | 1 | $8.47835326(19) \times 10^{-30}$ C·m |
| Magnetic field | 1 | $2.35 \times 10^{5}$ T |

Table 1.1: Atomic units

## 1.3 Dissertation Structure

Subsequent chapters describe the experimental approach, simulation and several independent projects. Each project contains both experimental description and simulation description. But more details and common parts of all experiments will be found in Chapter 2 and Chapter 3.

Chapter 2 provides the information about experimental setups. It introduces the apparatuses commonly used in the experiments, as well as the daily operation. More details about some instruments could be found in manuals and dissertations from previous students who worked in this lab. The purpose of Chapter 2 is to give same ideas about the apparatuses and operations in the lab.

Chapter 3 talks about physics concepts commonly involved in the experiments, and their mathematical expression in simulation. There's no way to put every single simulation code in this dissertation, but by following the models described in Chapter 3, one could reconstruct the simulation result in a fairly easy way.

Chapter 4 is describing the work which denies the collective decay in a cold Rydberg gas. From our experience of daily operation of cold Rydberg atoms, we did not observe any proof for superradiance, which is claimed to be observed by some other group. We did detailed researches into this topic and provided explanations of our observation.

Chapter 5 is exploring the wavepackets evolution in dipole-dipole coupled atoms. It proves, through experiment and simulation, that in dipole-dipole coupled atoms, the wavepackets are not evolving independently, their oscillation decays with the existence of the dipole-dipole interaction instead.

Chapter 6 discusses the coherence transfer between atoms through dipole-dipole interaction. It provides experimental results which show that there is coherence transfer between atoms with the existence of dipole-dipole interaction. Simulation shows that dipole-dipole interaction can cause the coherence transfer, but some conditions have to be satisfied to get good results.

Chapter 7 summarizes the work done in this dissertation and briefly discusses the work in the future.

# 2 Experimental Setup

This chapter contains the general experimental setup for researches discussed in this dissertation. It introduces the setup for state excitation, laser cooling, pulse amplification, Tera Hertz (THz) pulse generation, data collection and etc. It also provides some suggestion for maintenance and daily operation. All experiments are performed on Newport RS 3000 optical tables to reduce mechanic vibrations, in a temperature controlled room to reduce external thermal fluctuation. Other than specifically noted, the repetition rate of all experiments is 15 Hz. Before getting into experiments in the lab, people are supposed to have already taken the safety training.

## 2.1 Magneto-Optical Trap

Since its invention in 1987 [1], Magneto-Optical Trap (MOT) has become a very important and popular technology in the area of atomic research and has been widely used to generate cold neutral atoms. This technology is a combination of magnetic field gradient and counter-propagating laser beams. Gradient magnetic field is used to generate position dependent energy levels of atoms so that atoms not in the trap center would absorb specially prepared photons of fine-tuned lasers and be pushed back to the center by scattering photons in random directions.

Due to its ease of operation and low cost, MOT has been used to trap cold atoms in all the experiments described in this dissertation. We use $^{85}$Rb as the atom source in all experiments. A MOT system contains high vacuum chambers, pump and repump lasers, pressure gauges, atomic beams generation and etc. Since Mary has already given a very good and detailed description about this system [3], a simplified version will be provided here.

### 2.1.1 Principle of Magneto-Optical Trap

A simplified one-dimensional two-state system can help to understand the cooling process. As shown in Figure 2.1, suppose one atom has a spin $S = 0$ ground state and a spin $S = 1$ excited states. In the one-dimensional system with axis $z$, the weak inhomogeneous magnetic filed varies linearly so $B_z(z) = Mz$ where $M$ is a constant. Due to Zeeman effect $\Delta E = \mu m_s B = \mu m_s M z$ , this field splits the degeneracy of the excited states. creating positon dependent energies for the atoms.  In the system, a beam of $\sigma_-$ light propagates in the $-\hat{z}$ direction and anther beam of $\sigma_+$ light propagates in the counter direction. Both beams are red detuned from the zero-field resonance. On one hand, an atom with a position

$z > 0$ is more likely to absorb photons from $\sigma_-$ to jump from ground spin state to $m_s = -1$ state since $m_s = -1$ state is closer to resonance. On the other hand, an atom with a position $z < 0$ is more likely to absorb photons from the $\sigma_+$ to jump from ground spin state to $m_s = 1$ state. The atom absorbs a photon and is pushed back to the center. It will then scatter the absorbed photon. But as long as the field is weak, the scattering direction is random, which generates a net force of pushing back on the atom. So the atom will be cooled and confined in the MOT.
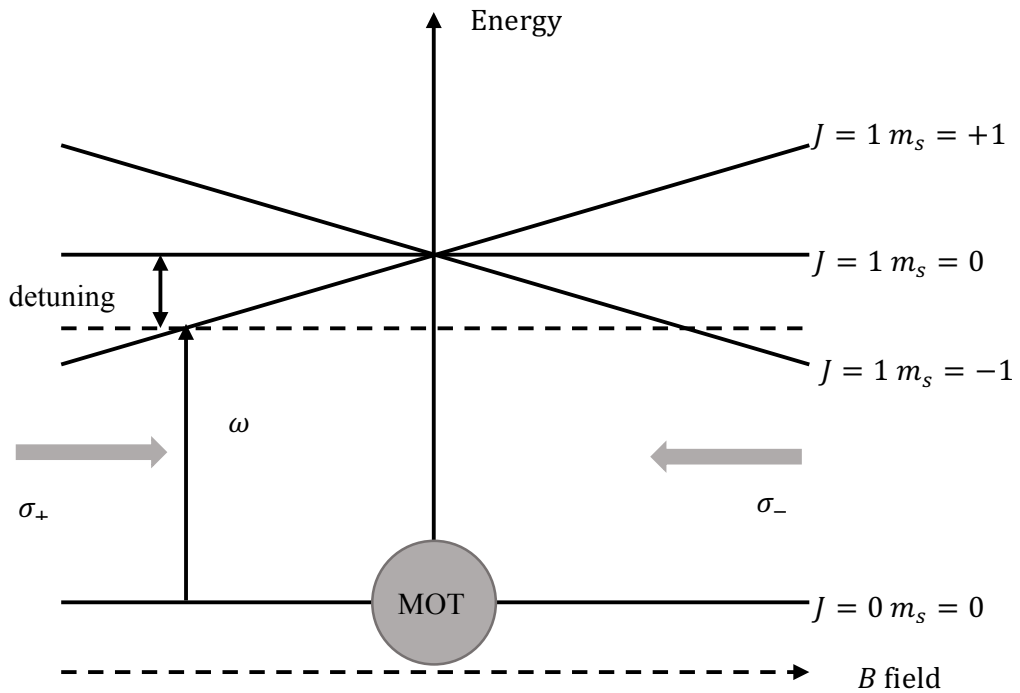


Figure 2.1: Simplified one dimensional model for MOT [2].

As shown in Figure 2.2, a three dimensional Magneto-Optical Trap is similar to one dimensional model. The gradient magnetic field in a three dimensional MOT is provided by anti-Helmholtz coils. Other than the two main anti-Helmholtz coils as shown in this schematic, there are six more shim coils which enable fine tuning of the magnetic field inside the MOT. The six laser beams are from the same laser head. We use three beam

splitters to split the main beam into three with equal strength. These three beams are then reflected by mirrors to generate six counter-propagating beams in total. Before reflected back, the beams polarizations are rotated by waveplates placed in front of the mirrors.
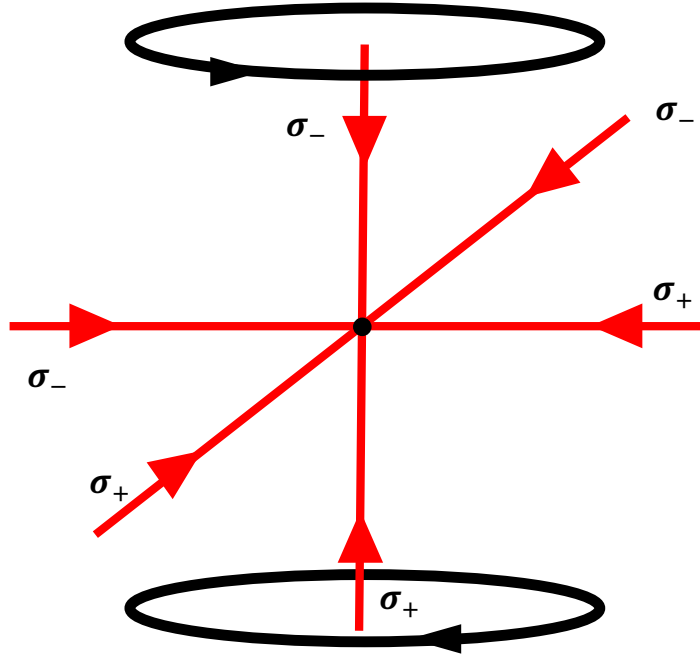


Figure 2.2: Schematic for MOT design. It's a combination of anti-Helmholtz coils and six counter-propagating beams.

The above discussion gives an idea about trapping two-level atoms. When dealing with $^{85}$Rb, there are more states involved, although the basic principal is as same as described above. As shown in Figure 2.3, there are complicated hyperfine levels involved in a realistic MOT. The ground state has been split into two hyperfine levels F = 2 and F = 3. The excited state has been split into four hyperfine levels F = 1, 2, 3, 4. Ideally, the trap laser intends to transfer atoms from $5s_{1/2}$ F = 3 to $5p_{3/2}$ F = 4. But because $5p_{3/2}$ F = 3 and $5p_{3/2}$ F = 4

are so close that the trap laser transfers a portion of atoms to $5p_{3/2}$ F = 3. The atoms in

$5p_{3/2}$ F = 3 decay quickly back to $5s_{1/2}$ F = 2 and escape from the MOT. To avoid such a

loss, a second repump laser is introduced into the system. The repump laser transfers the

atoms in $5s_{1/2}$ F = 2 back to $5p_{3/2}$ F = 3. These atoms can later decay back to $5s_{1/2}$ F = 3

and be transferred again by the trap laser.
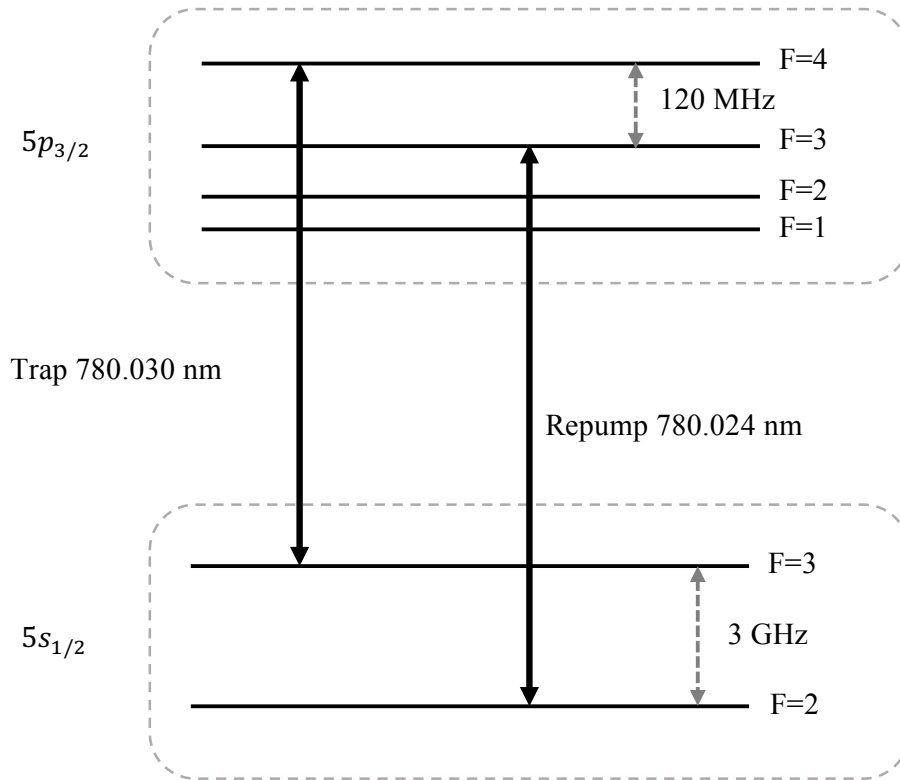


Figure 2.3: Hyperfine energy structure of $^{85}$Rb. Trap laser is driving transition from $5s_{1/2}$
F = 3 to $5p_{3/2}$ F = 4 and repump laser is driving transition from $5s_{1/2}$ F = 2 to $5p_{3/2}$ F = 3.

## 2.1.2  Saturated Absorption Spectroscopy

To find the well defined frequency for the trap laser and repump laser, we utilize a

method called Saturated Absorption Spectroscopy or SAS. The basic idea is this:

1. Split a small branch from the main beam of the laser. The function of this branch is to help find the right frequency. Pass it through a cell containing rubidium vapor. Call this branch "pump" beam. It's strong enough to saturate the absorption along the path.

2. Reflect back the pump beam and pass it through the cell again. Call the coming back beam "probe" beam.

3. Detect the probe intensity using a photo detector. If the beam frequency is a little off the well defined frequency, due to Doppler effect, the atoms in the cell will absorb both pump and probe beams. If the beam frequency is right the well defined frequency, only zero-velocity atoms can absorb photons from the pump beam. The probe beam would not decrease its intensity since the pump beam has already saturated the absorption. Thus there will be an intensity increase of the probe beam when the frequency of the beam is the right the Doppler-free frequency.

In the experiment, the real setup is a little more complicated than the above description. The beam passing through the cell has been split further into two beams. One comes back as a probe and the other is detected directly. The detected signal from the probe is then subtracted by the signal from the other beam, which creates a push-pull configuration. In this way, we can get rid of the fluctuation of the main beam intensity and stabilize the absorption spectrum.

The right spectrum for trap and repump lasers are shown in Figure 2.4. It's generated by sweeping the piezo voltage of the laser head with a tringle or sine wave. The pump beam from the trapping beam has been increased by 36 MHz using an acousto-optic modulator (AOM) before being sent to the cell. In this way, the main trapping beam sent into the MOT is detuned by 36 MHz.

Once the right spectrum pattern has been found, lock the lasers.
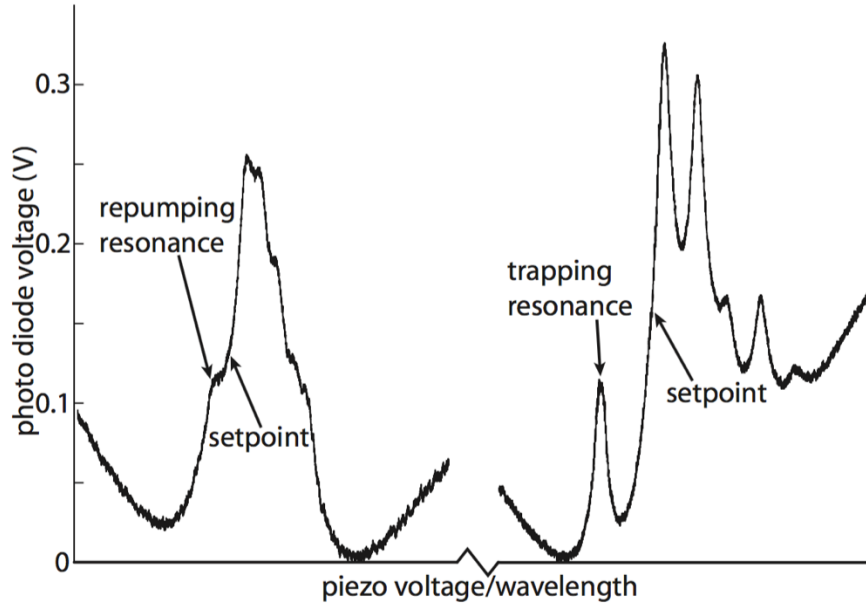


Figure 2.4: Plots of the saturated absorption spectrum near the repumping and trapping resonances.[3]

## 2.1.3  Ultra High Vacuum Chamber

The MOT is sitting inside an ultra high vacuum chamber. When pressure goes higher, because of the collision by high speed atoms, less atoms will stay in the trap. The usual operation pressure is between $10^{-10}$ torr to $5 \times 10^{-9}$ torr. To achieve such a low pressure, a serial of pumps: rough pump, turbo pump and ion pump have been utilized. It does not need to use all of these pumps often, but if needed, Hyunwook has given a detailed description of the operation of these pumps for reference [4].

The pressure in the UHV chamber is measured by two types of gauges: thermocouple and Bayard-Alpert ionization gauges, both of which are monitored by Varian senTorr gauge.

The thermocouple gauge measures pressure from $10^{-3}$ to $10^2$ torr, while Varian senTor gauge can measure as low as $2 \times 10^{-11}$ torr. The ion pump can also display the pressure and we usually refer to that reading for daily operation.

## 2.1.4 Performance of the MOT

The temperature of the atoms trapped in the MOT can go down as low as about 70 $\mu$K. Mary discussed the details to measure the atom's temperature and calibrate the density of atoms trapped in the MOT [3]. A brief introduction of the method is provided below.

Before getting temperature or density, we need to get the diameter of the atom cloud. This is done by producing a thin horizontal "film" of excitation laser beam which will excite all the atoms in the film from $5s_{1/2}$ to $5p_{3/2}$ and then to $5d$. The ion signal is correlated with the atoms distributed in the vertical direction. Using the same method and we can then find the atoms' horizontal distribution, which should be the same as the vertical distribution if the MOT is ideally round. Using Gaussian curve to fit the distribution and we can get the diameter of the MOT. A typical MOT has a FWHM from 0.4 to 1 mm.

The basic idea for temperature measurement is to turn off the trapping beam and observe the expansion of the atom cloud, since there is a correlation between temperature and expansion rate according to Boltzmann distribution: $\Phi(v_x) = \sqrt{\frac{m}{2\pi kT}} e^{-\frac{mv_x^2}{2kT}}$.

The basic idea for measuring atom number in the could is to measure the total power scattered from the cloud or the fluorescence $P_{total}$. The scattered power contributed by an individual atom, which decays from $5p_{3/2}$ to $5s_{1/2}$ once every two natural lifetime, $P_1$ is calculated by

$$P_1 = \frac{hc}{\lambda} \frac{1}{2\tau} \tag{2.1}$$

where $\lambda$ is the wavelength of the scattered photon and $\tau$ is the natural lifetime. Then we can get the total atom number:

$$N = P_{total}/P_1 .$$
( 2.2)

## 2.2 Lasers and Amplifiers

### 2.2.1 Nd:YAG Lasers

Nd:YAG lasers are one kind of solid state lasers. The lasing medium in this laser is neodymium-doped yttrium aluminum garnet (Nd: $Y_3Al_5O_{12}$ or Nd: YAG). Such a medium is pumped by flash lamps and absorbs mostly in the bands between 730–760 nm and 790–820 nm [5]. It then emits light which mostly centered at 1064 nm. When the laser pulses fire is controlled by flash lamps and Q-switch [refer to Figure 2.6]. The infrared output is not very useful either for directly pumping dye lasers or exciting atoms in our experiments, but it can be used to generate beams of other frequencies. For the experiments described in later chapters, Potassium Dihydrogen Phosphate (KDP) crystals are used to generate 2nd or 3rd harmonics of the source frequency. 2nd and 3rd harmonic lasers are centered at 532 nm and 355 nm respectively. The green light at 532 nm is used to pump Regenerative amplifier,

linear amplifier and dye laser. The ultraviolet light at 355 nm is commonly used to pump

dye amplifiers.
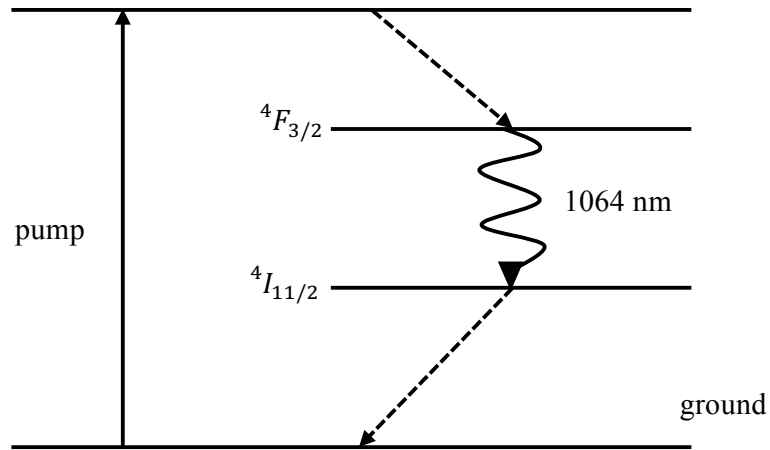


Figure 2.5: Schematic of Nd:YAG transition [6]. It is a typical Four-level Transition

Scheme.
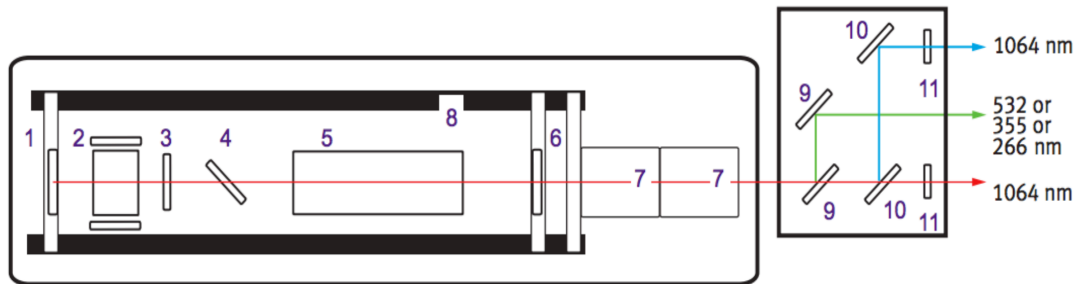


1 Rear Mirror, 2 Pockels Cell, 3 $\lambda/4$ Plate, 4 Dielectric Polarizer, 5 Oscillator Rod, 6
Gaussian Output Coupler, 7 Optional Harmonic Generators, 8 Graphite Resonator
Structure, 9 Dichroic Separation, 10 1064 nm Mirrors, 11 Beam Block

Figure 2.6: Layout of Continuum Surelite Nd:YAG laser. It can output beams of 4 different

frequencies.

One Nd:YAG laser combined with KDP can generated $2^{nd}$ and $3^{rd}$ harmonics at the same time. But some experiments require more $2^{nd}$ and $3^{rd}$ harmonics at different times. So there are two Nd:YAG lasers used in the lab. One is Spectra-Physics GCR-100 Series. Its function is to generate 532 nm green light. This green light is the pump light for Regenerative Amplifier and Linear Amplifier, both of which will be discussed in following content. The other one is Continuum Surelite and it's used to generate ultraviolet light. It's used to pump dye lasers and dye amplifiers in the experiments.

## 2.2.2  Diode Lasers

Diode lasers are lasers using a *p-n* junction or a *p-i-n* structure to generate gain. Semiconductor components are usually compact so diode lasers are commonly used in space-limited cases. Another advantage of diode lasers is that their output frequency is tunable. The cavity of a diode laser is controlling by a small grating in the diode laser head and the grating is usually attached to a piezo. By changing the voltage applied on the piezo, it is convenient to tune the output frequency. In the experiments, following diode lasers are used:

- Vortex tunable diode lasers from New Focus. Continuous Wave or CW laser. Typical output frequency is 780 nm and output power 40 mW. They are used as trap and repump lasers for the Magneto-Optical Trap.

- Millennia Vs diode laser from Spectra-Physics. CW laser. Typical output frequency is 532 nm. It's used as the pump of seed light.

- TA-SHG pro High Power Frequency-Doubled Tunable Diode Laser System. CW laser. Typical output frequency is 490 nm and output power 150 mW. It's used to generate Rydberg excitation pulses.

## 2.2.3  Mode Lock Lasers

Mode locked lasers are commonly used to generate ultra short laser pulses. A mode locked laser is a laser to which the technology of mode locking is applied. A bunch of different independent oscillations with different frequency components in a cavity could not compose a pulse, since there is no fixed phase between each other. But if the phase between each oscillation is fixed, these oscillations could generate intense bursts periodically or a train of pulses consistently. Such phase fixing process is the so called "mode locking" process, and there are two major ways to achieve the mode locking: active mode locking and passive mode locking.

The mode lock laser used in the experiments is model MTS mini Ti:Sapphire laser kit from Kapteyn-Muranen. It uses Kerr-lens mode locking technology which is one of passive mode locking technologies to mode lock laser. Its diagram is shown in Figure 2.7. When the CW pump beam going through the Ti:Sapphire crystal is not stable, because higher intensity light can pass the crystal easier than low intensity light, the cavity is in favor of high intensity light pulses. So the routine operation is to touch the $2^{nd}$ prism to produce disturbance to generate pulses. The outcome are pulses of light as short as sub 15 femtoseconds at a repetition rate about 90 MHz. The output pulse spectrum is monitored using a spectrometer. If the output is not mode locked, it is a CW beam and the spectrum is a line with no bandwidth. For well mode locked pulses, the spectrum is very stable and has a bandwidth. The narrowness of the output pulses is enough for our experiment but the power is too small. To get narrow pulses with large enough power, we use the pulses from the mode lock laser as "seed light" and amplify them. The amplification process is discussed in 2.2.4.
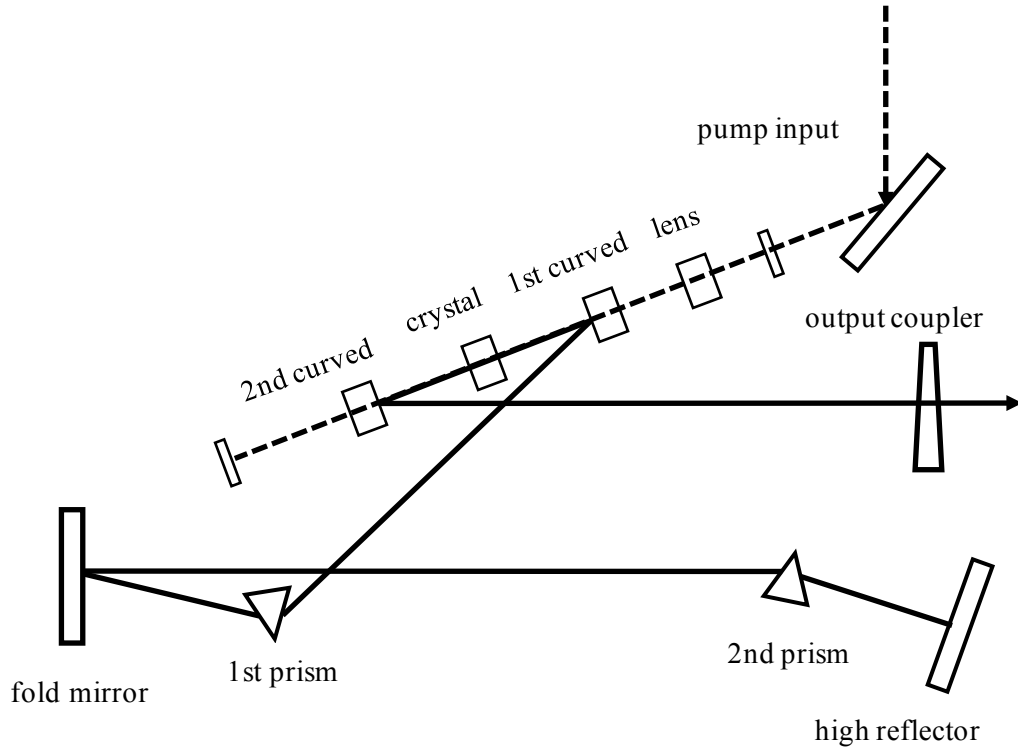
Figure 2.7: Basic layout of the mode lock laser [9]. Dashed line is the pump light from Millennia Vs diode laser and solid line is the oscillation in the cavity which is centered at 780-800 nm. By tapping the 2$^{nd}$ prism, we can produce a temporary unstable beam. Stronger intensity part in this beam will be enhanced thus produce pulsed outputs.

## 2.2.4  Chirped Pulse Amplification

As mentioned above, the output from the mode locked laser has very short duration but its amplitude is not large enough for the experiments. So the output beam from the mode lock laser or the so called "seed light" has to be amplified. This is achieved through a popular technology called "Chirped Pulse Amplification". The basic idea is this:

1.  Stretch the short pulses to a broad duration so that the peak energy is not very high. It's easier to amplify low energy peaks than high energy peaks. As shown in Figure 2.8, the combination of reflecting mirrors and a grating in the stretcher acts as a

pair of gratings and disperses the seed light's spectrum. By stretching the seed light pulse, the energy in each pulse is much smaller and it's much easier to amplify the pulse.

2. Amplify the stretched pulses using amplifiers such as regenerative amplifiers and linear amplifiers.

3. Compress the amplified stretched pulses to high intensity short pulses back using a compressor. Compressor acts as an opponent of a stretcher, but it also utilizes a grating. In the experiments, the compressor is adjusted to find the best performance of the Tera Hertz generation.
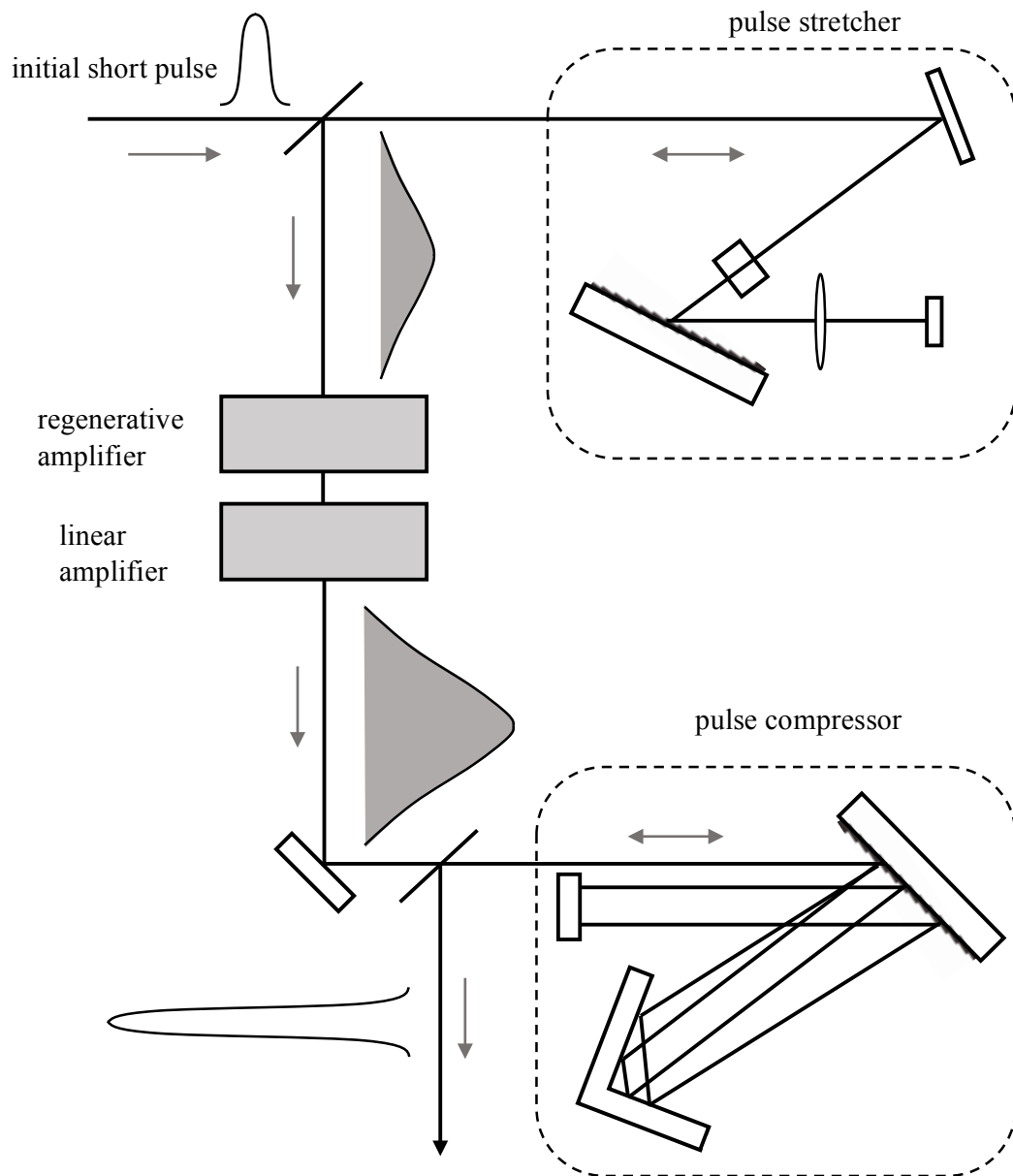
Figure 2.8: Schematic of chirped pulse amplification system. Seed light is at first stretched using stretcher. Then the stretched pulse gets amplified. At last the pulse is compressed to be very short pulse with high intensity.

## 2.2.5 Regenerative Amplifier

The first amplifier in the chirped pulse amplification is a regenerative amplifier. It use a solid-state medium Ti:Sapphire as the gain medium. Pulses are switched into the optical resonator by an optical switch realized with an electro-optical modulator and a polarizer, multiply pass through the gain medium in an optical resonator, get amplified, and finally are switched out by another optical switch. This schematic is shown in Figure 2.9. The input beam has a vertical polarization to the paper surface and is reflected by the first polarizer to the switch-in pockels cell. When the switch-in pockels cell is triggered, it works as a quarter waveplate and rotates the beam's polarization from vertical to horizontal before the beam comes back to the first polarizer. The beam with horizontal polarization goes through the first polarizer and comes into the gain medium to get amplified. After a few runs in the cavity (usually 5 to 6 runs) to gain maximum intensity, the beam will be switched out by the switch-out pockels cell with a vertical polarization.
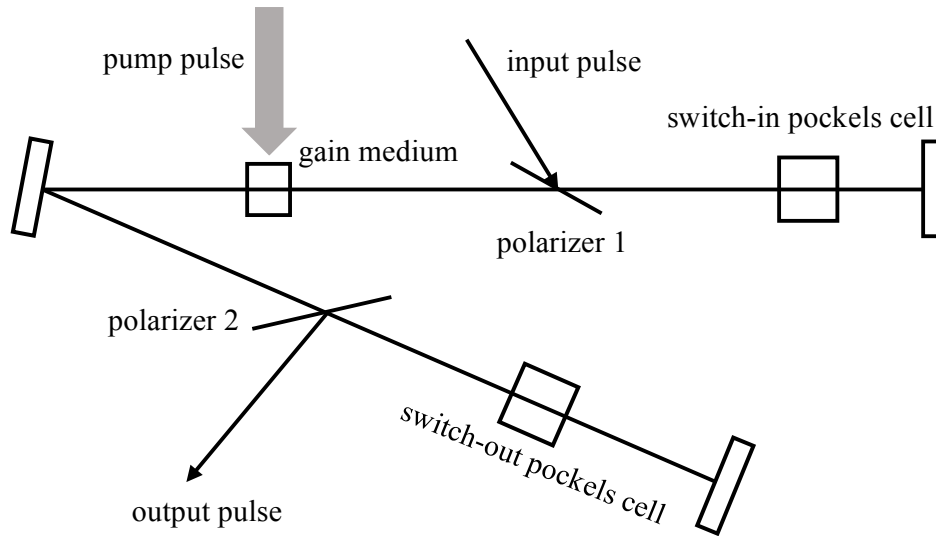
Figure 2.9: Schematic of regenerative amplifier. Switch in pockels cell controls when the pulse comes into the resonator and switch out pockels cell controls when the pulse comes out.

## 2.2.6 Linear Amplifier

Linear amplifier is used when the pulse intensity from the regenerative amplifier is still not large enough. A pulse also achieves the amplification by multiply passing through the gain medium Ti:Sapphire crystal, but it's relatively simpler than regenerative amplifier. The highest output from linear amplifier in our lab is over 600 mw. Its structure is shown in Figure 2.10.
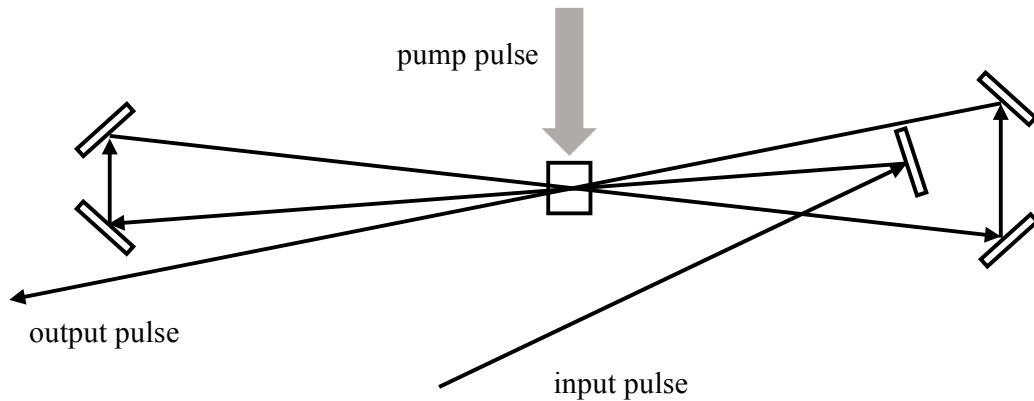
Figure 2.10: Schematic of linear amplifier. Beam passes the gain medium multiple times and gets amplified.

## 2.2.7  Dye Laser and Dye Amplifier

Different from Nd:YAG laser, which is a solid state laser, a dye laser is a laser which uses an organic dye as the lasing medium, usually in a liquid solution. Its advantage, compared to solid state lasers, is that it can be tuned for a much wider range of wavenumbers. The wide bandwidth makes it particularly suitable for tunable lasers and pulsed lasers. (At the same time, its disadvantage is the frequency instability.)

Organic dye is dissolved in solvent and circulated through a dye cell which is shot by pulsed pump light. When it's excited by pump light, it fluoresces over a range of wavelengths. Certain wavelengths will be stimulated when the dye cell is placed in a cavity and thus a laser will be generated. By changing the cavity, the frequency which is to be stimulated, is tunable. This is the basic idea of dye lasers.

There are two main styles of dye lasers. One is Hansch-style and the other Littman-style. In our experiments, only Hansch-style dye laser [7] has been used for Rydberg excitations.
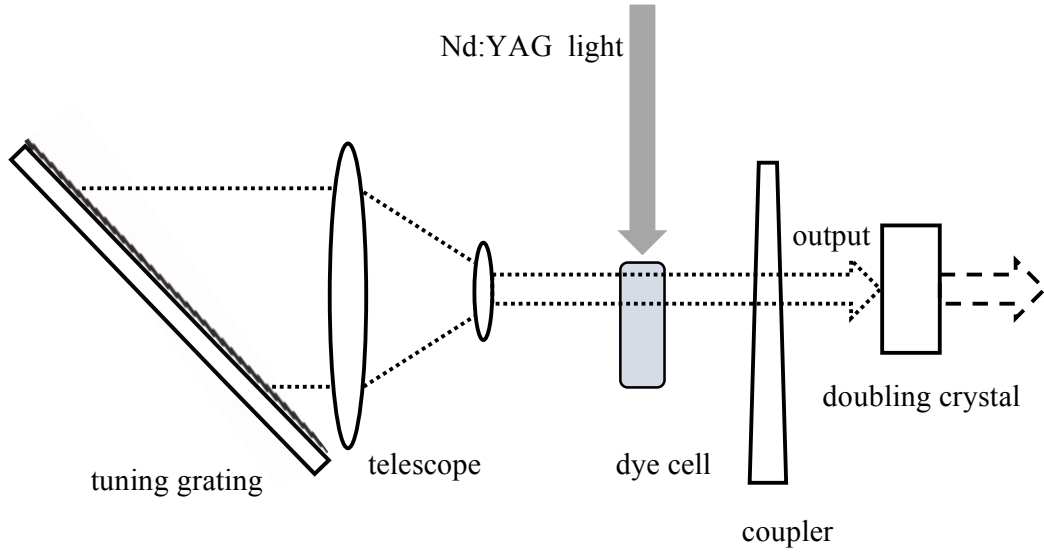
Figure 2.11: Schematic for a Hansch dye laser and $2^{nd}$ harmonic generation. The angle of the tuning grating determines the output frequency.

This dye laser is used to generate $25s$ Rydberg atoms. The proper laser dye is LDS 925, which is dissolved in methanol solvent, with a concentration of 250 mg/L. This solution is pumped by $2^{nd}$ harmonic from Continuum Surelite. The pump light has been focused about a millimeter into the dye cell by a cylindrical lens, creating a line of gain medium across the face of the cell. The dye cell works as a fluorescence generator, as well as an amplifier. The telescope expands the beam to reduce the intensity of light on the tuning grating. The grating is rotatable, which determines the frequency of the light diffracted back to the cavity.

The light then comes back to the dye amplifier, being amplified and escapes from the cavity. Its infrared output laser is then frequency doubled to generate blue pulses which frequency is centered at about 486 nm. For most of the time, a pulse from the dye laser does not only contain the frequency we want but a broad range of wavelengths. A typical line width for this kind of dye laser is on the order of 1 cm$^{-1}$. To reduce the line width, we usually put a bandwidth filter or an etalon before sending the beam into the MOT chamber. In the chamber, the beam drives Rb atoms from $5p$ state to $25s$ state.

The dye cell can also work separately as an amplifier in Figure 2.12. This double amplifier can be used to amplify seed light from other lasers. We do not know exactly the output power of light coming from the dye amplifier, but we make sure the state transition is saturated by the amplified laser beam. If there is no observable reduce of the population on a state such as $25s$ when inserting a 20% beam reducer in the path, we are confident that the state transition is saturated and the power of the beam is large enough.
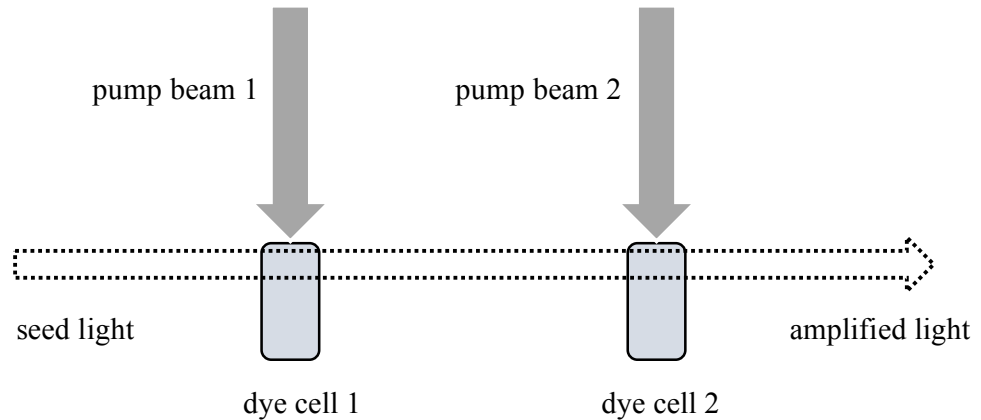


Figure 2.12: Schematic for double cell dye amplifier used in the lab.

## 2.3 Tera Hertz Pulses

### 2.3.1 Tera Hertz Generation

Tera Hertz (or THz) pulse generated in our lab are pulses with a frequency of the order of Tera Hertz and the duration a few ps.

This work will be updated later.

## 2.4 Detection and Data Collection

### 2.4.1 Selective Field Ionization

In some experiments, we want to detect wavepackets. But wavepackets cannot be detected directly. Instead, state distribution has been detected to reveal the wavepacket dynamics. As an efficient state distribution detection technology, Selective Field Ionization has been used to widely [8].

The highest electron is trapped in a $1/r$ potential trap in alkali atoms. When an offset field is applied to the atom, the trap will be tipped as shown in Figure 2.13, which lowers the barriers trapping the electron. When the barrier is low enough, the electron would be able to escape from the trap. During the tipping process, higher state electrons tend to be ionized earlier than low state electrons.

In the MOT chamber, there are four metal rods. Two of them are connected to high voltage pulse supply and the other two are connected to ground or low static voltage. These 4 rods create a strong electric field which gets maximum in 1 $\mu$s (slow ionization field) or 500 $n$s (fast ionization field). Atoms in this field will be ionized and the ions will fly to a

detector composed of micro-channel plates (MCP). Atoms in different states are ionized at different times, so the electric signal have different arrival time thus the population of states can be distinguished.
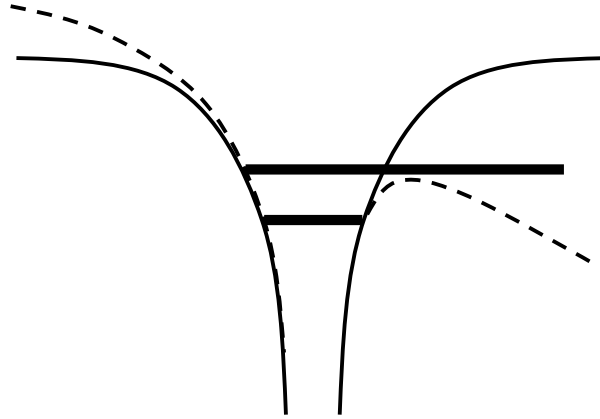
Figure 2.13: Schematic of the tipping of electron potential. Solid line is the $1/r$ potential when there is no external field applied to the atom. Dashed line shows the tip of potential when a filed is applied to the atom. When such a field is strong enough, electrons are able to escape from the trap.

## 2.4.2 Synchronization System

Before taking any measurement, we have to make sure the timing is right. The timing is controlled by a synchronization system in the lab. It's a combination of clocks, delay generators and synchronization boxes. The principal behind such a system is that it's flexible enough to adapt to changes. Figure 2.14 shows the synchronization system working in the experiment described in Chapter 6. A little changes need for this system to work for other experiments. "Master" is a divider which divides the commercial 60 Hz electricity

supply by 4 and provides a 15 Hz source to trigger a digital delay/pulse generator, Model

DG535 from Stanford Research Systems, INC. One channel of this delay generator will be

the trigger of another DG535 which controls the time of firing the lamps inside Surelite

Nd:YAG laser. Another channel will trigger the lamp of GCR-100 Nd:YAG laser. The

GCR-100 will provide a "ready" signal when the lamp is outputting power. This signal is

synchronized in the SM-1 synchronization box with one pulse from the seed light. SM-1

outputs trigger signals for DG645 and another DG535. DG535 controls the Q-switch of

GCR-100 Nd:YAG and pockels cells in the Regenerative Amplifier to get seed light

amplified. DG645 controls the Q-switch of Surelite Nd:YAG, the ionization filed, scopes

and etc. The delays are easy to change on these delay generators so this system can handle

different timing for different experiments.
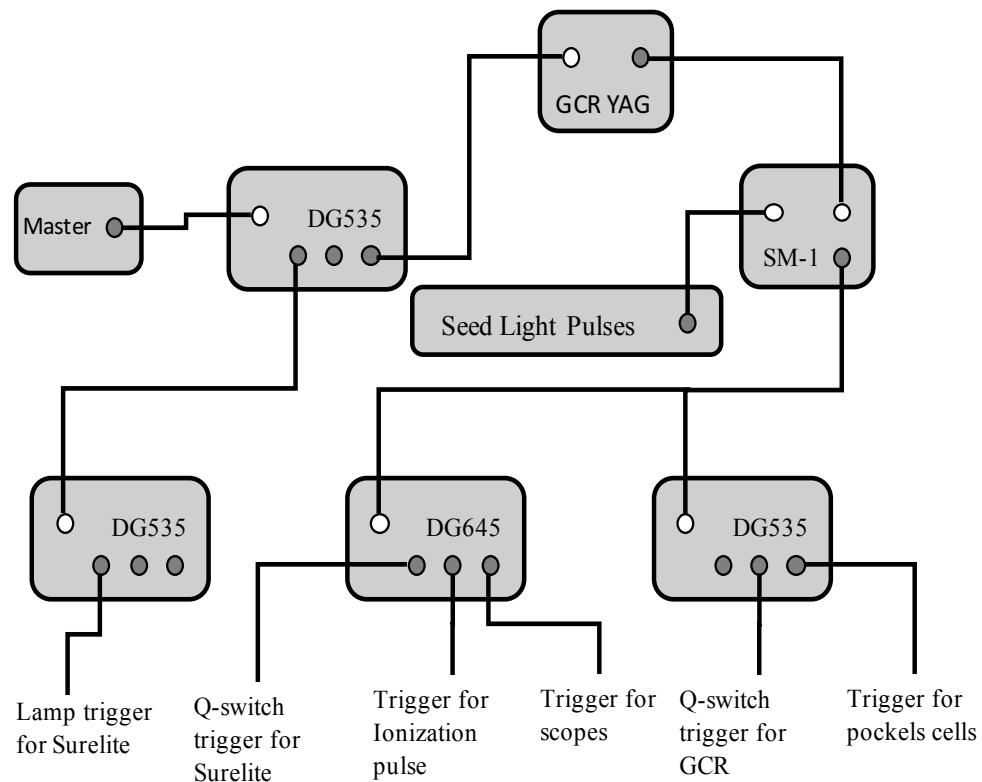


Figure 2.14: Schematic of the Synchronization System. White cycles are inputs and dark

cycles are outputs.

## 2.4.3 Measurement Operation

The electric signal from MCP is collected using oscilloscopes. And the oscilloscopes transfer the data on the screen to computers which is using programs written in Labview. A typical electric signal representing a state population is a peak with some width. Usually, the larger a state population is, the higher the peak is. But the height is not an accurate value to measure the population. Instead, the area of peak is proportional to the state population. As show in Figure 2.15, the main peak crossed by a gate is the ionization signal of states. When there is no ionization signal, the peak will disappear and there is only background left. Using the program written in Labview, we can easily measure the area under the peak in the gate. After subtracting this area by the area when there is only background, we can get the real area representing the excitation population. As the population changes, the integrated value in the gate changes accordingly.
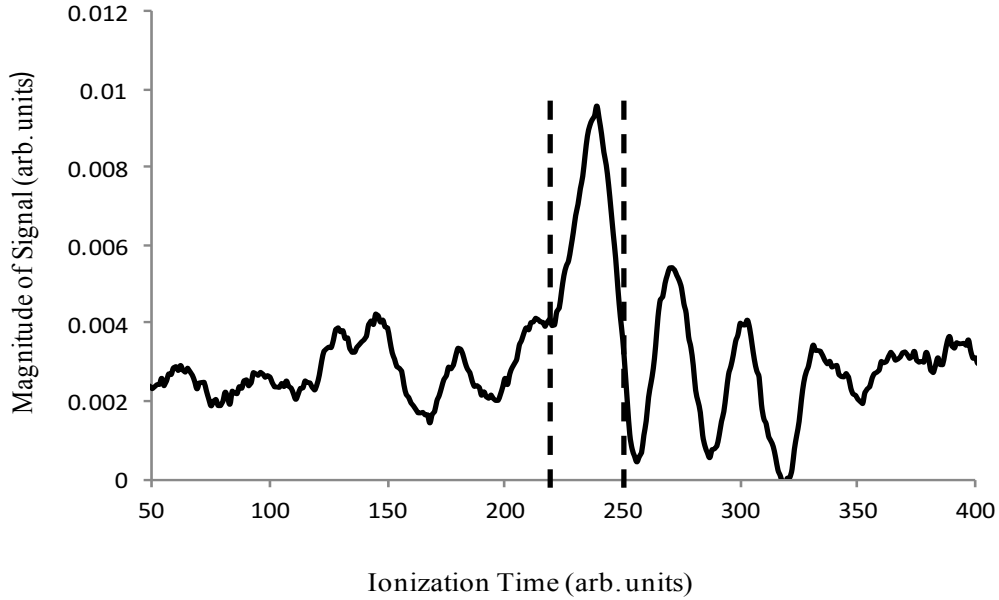


Figure 2.15: A typical ionization signal shown on an oscilloscope. The central peak representing the population of state $32s + 32p$. The measurement program puts a gate across the peak and integrates the area under the peak in the gate.

# 2.5 Maintenance and Daily Operation

Before doing experiments, people should have finished the safety training.

Before turning on lasers, internal lock switch has to be flipped on. It controls the interlock of most lasers in the lab. When the switch is on, a red bulb outside the lab will be on to give a warning signal.

## 2.5.1 Daily Examination

1. Check the MOT chamber pressure. The reading from the ion pump should be no more than orders of $10^{-8}$ torr. If the pressure is higher than this reading, there might be some leakage.

2. Check pressure of canned nitrogen which is used to keep GCR-100 laser head clean and dry. The inner pressure should be higher than zero and the output pressure should be around 5 psi. From previous experience, the nitrogen needs to be replaced every two to three weeks.

3. Check the room temperature readings. The readings should be from 72 $^0$F to 74 $^0$F. For some extreme climates, the temperature may be out of this range.

4. Check temperature of cooling water from external sources. The supply water should have a temperature around 60 $^0$F.

5. Check cooling water level for each laser before turning on the laser. The water level should be in the proper range marked in the box.

6. Check the fume hoods to make sure they are working properly.

## 2.5.2  Operation of Regenerative Amplifier

Turn on the seed light pump laser power switch. When the temperature is stabilized, turn on the laser. The pump should be in mode "power" and the setup for power is "3.75 W" shown on the display screen.

1. Let the pump laser warm for at least half an hour. Then lock the mode. If the mode lock is not very stable, usually it's because the alignment of the seed light is off and it needs adjustment.

2. Turn on the regenerative pump GCR-100 Nd:YAG laser. Slowly increase the power of the pumping lamp until it reaches the maximum. It usually takes several seconds or minutes for the dimmer light to turn on. If it takes too long, it's probably because there are two many ions in the cooling system and the charge of lamps is not working properly. Reflush the cooling system using deionized water if that happens and try again.

3. Let the Nd:YAG laser warm for at least one hour to acquire thermal balance.

4. Change the output pockels cell's timing to be the long timing set, which is 4us longer than the short timing set (which should be almost the same every day). This is to enable self lasing of the amplifier. Switch on all the pockels cells in the setup. Increase the Nd:YAG pump light to be a little higher than the threshold. (The threshold may vary a little bit every day. The recent value should be marked down in the log book.)

5. There should be a bright spot showing in the TV monitor, which means the regenerative amplifier is now lasing itself. If there is no bright spot, increase the pump light a little higher but not larger than the normal pump level. Adjust the coupling mirrors to make sure the threshold is minimized.

6. Block the pump light. Change back the output pockels cell's timing to the short timing set. Increase the pump light to the ordinary operation level (which is also written down

in the log book). Unblock the pump light. Now on the scope, there should be a stably increasing pulse train.

At this point, Regenerative amplifier is ready. Fine tuning includes decreasing the threshold and making the pulse train more stable. The pump Nd:YAG laser needs to replace lamps every 700 hours under current repetition frequency. The normal output and the last replacement date are marked underneath the laser head on the optical table.

## 2.5.3 Operation of MOT

1. First turn on the cooling water waives. Check the flow meter to make sure cold water is flowing through the coils' cooling tubes. If there is no flow or the flow is too slow, power supplier of the main anti-Helmholtz coils should not be turned on. Check the paddle wheel monitor to make sure water can flow. The normal in pressure is 14 psi. Make sure there is no leakage of water from the cooling tubes.

2. Turn on diode lasers of trap and repump beams.

3. Turn on AOM driver, voltage ramp of the diode grating, scopes, TV monitors and power supplies of coils. Increase the output of the power supply of the main coils to 10V. The resistance of the main coils is 1 ohm, so the output current of the power supply should be around 10A.

4. Turn on the getter and slowly increase it to the operating value. A normal operating current is from 1.9 A to 2.5 A. When this value has to be as large as 3.5 A to generate an observable cloud of atoms shown on the TV monitor, it means the getter has been used up. Under ordinary usage, this process could take about 4 to 5 years. Once the getter has been used up, it should be replaced by a new one.

5. Let the trap and repump lasers warm for at least one hour to achieve thermal balance. Then adjust the piezo voltage of the lasers to find the right absorption signal. If the

absorption signal is no way similar to the proper pattern, use a spectrometer to check the output frequency. For the trap laser, the output frequency range should cover the value 384232.6 GHz and for the repump laser 384231.2 GHz. If a diode laser could not reach the required value, it is possible that the piezo in the laser head is damaged and needs to be replaced. Lock lasers.

At this point, there should be a bright spot shown on the TV monitors. It's the scattered infrared light from the cold atom source. A good MOT on the screen is a bright stable spot with a clear circular shape. If the spot is not stable or the shape is not round, the first step to try is to adjust the shim coils to make it good. If the shim coils do not do the work, more dedicated adjustments of the laser beams are necessary.

# Bibliography

[1] E. L. Raab, M. Prentiss, Alex Cable, Steven Chu, and D. E. Pritchard. Trapping of Neutral Sodium Atoms with Radiation Pressure. Phys. Rev. Lett. 59, 2631 (1987).

[2] Harold J. Metchalf and Peter van der Straten. Laser Cooling and Trapping. Springer (1999).

[3] Mary Kutteruf, Coherence in Rydberg Atoms: Measurement and Control, PhD thesis, University of Virginia (2010).

[4] Hyunwook Park, Observation of the Dipole-Dipole Interaction Between Cold Rydberg Atoms by Microwave Spectroscopy, PhD thesis, University of Virginia (2012).

[5] Continuum, Mountain View, CA. Operation and Maintenance Manual for SureLite Lasers (1997).

[6] Spectra-Physics, Mountain View, CA. Pulsed ND:YAG Lasers User's Manual GCR-100 Series GCR-200 Series (1993).

[7] T.W. Hansch. Repetitively Pulsed Tunable Dye Laser for High Resolution Spectroscopy. Applied Optics, 11:895 (1972).

[8] Thomas F. Gallagher. Rydberg Atoms. Cambridge University Press 1994.

[9] Kapteyn-Murnane Laboratory Inc, Model MTS Mini Ti:Sapphire Laser Kit Instruction Manual 2003.

# 3 Models in Simulation

This chapter introduces general knowledge about the physical models used in the research. These models include Rydberg Atoms, Two-Body Model, Dipole-Dipole Interaction Model, Blackbody Radiation and etc. They are also expressed in math language so that they compose a mathematical background for the simulation implemented in Chapter 4, Chapter 5 and Chapter 6. Other than specifically noted, all the units in this chapter are atomic units.

## 3.1 Rydberg Atoms

Back to 1885, Balmer found the wavelengths of the visible series of atomic H is given by [1]:

$$\lambda = \frac{bn^2}{n^2 - 4} \qquad (3.1)$$

where b = 3464.6 Å. We now know equation (3.1) is the formula for the wavelengths of the Balmer series of transitions from the n = 2 states to the higher lying levels.

After quantitatively describing the wavelengths from H, people started to work on other atoms to unravel the mystery of atomic spectroscopy. Living and Dewar found that the observed spectral lines of Na could be grouped into different series [2]. Hartley found the significance of describing Balmer's formula in terms of the wavenumber of the observed lines instead of the wavelength during his reach on spectra of Mg, Zn, and Cd [3]:

$$\nu = \frac{1}{4b} \left( \frac{1}{4} - \frac{1}{n^2} \right). \qquad (3.2)$$

Now it's more clear what Balmer discovered reflects the energy difference between the $n$ = 2 states and the higher lying levels.

Following those precedents' work, Rydberg began to classify the spectra of other atoms, notably alkali atoms, into sharp, principal, and diffuse series of lines [4]. He found the wavenumbers of lines connoting the $s$ and $p$ series, for example, are given by:

$$\pm \nu = \frac{Ry}{(m - \delta_s)^2} - \frac{Ry}{(n - \delta_p)^2} \qquad (3.3)$$

where + sign and constant $n$ describe a sharp series of $s$ states and the minus sign and a constant $m$ describe a principal series of $p$ states. If $\delta_s = \delta_p = 0$ and $m = 2$ we can get Balmer's formula for the H transition from $n = 2$.

Due to his significant contribution, people are now naming atoms in states of high principal quantum number "Rydberg Atoms".

## 3.1.1  Modern Model of Rydberg Atoms

If we consider Rydberg states of H and Na, as shown in Figure 3.1, they are essentially similar. The only difference is that Na atom has a core which is composed of 11 positive charges and 10 electrons. For most of the time, the highest external electron (Rydberg electron) is far from the core and the difference between Na, H and all Rydberg atoms is trivial. But when the Rydberg electron comes near the core, it can both polarize and penetrate the $Na^+$ core, and change the wavefunctions and energies of Na Rydberg state from their hydrongenic counterparts.

(a)

$e^-$

$H^+$

(b)

$e^-$

$Na^+$
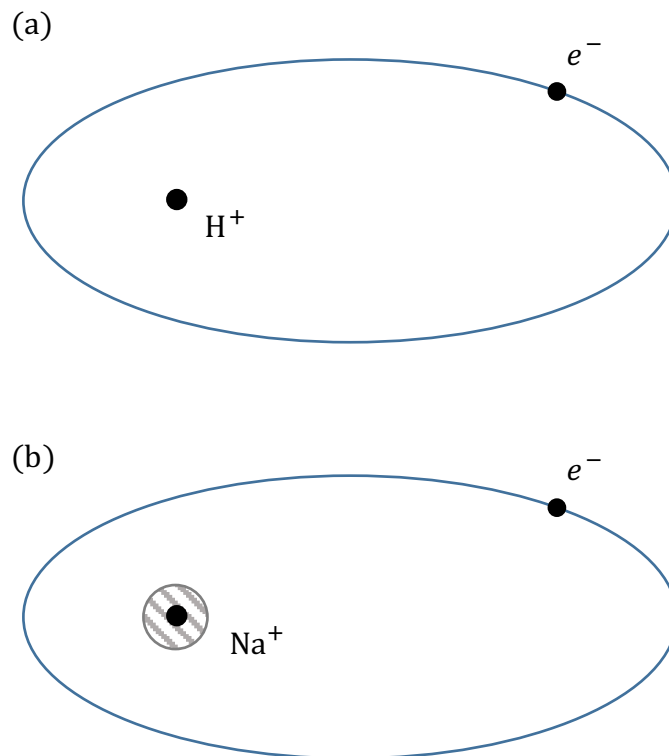
Figure 3.1: Rydberg atoms of (a) H and (b) Na. In H the electron orbits around the point of charge of the proton. In Na it orbits around the +11 nuclear charge and ten inner shell

electrons. In high l states Na behaves identically to H, but in low L states the Na electron penetrates and polarizes the inner shell electrons of the $Na^+$ core [5].

We know how to calculate wavefunctions of H [6]. This process can be easily extended to generate wavefunctions for single valence electron atoms with spherical ionic cores. Such an approach is called Quantum Defect Theory [7]. Quantum Defect Theory (QDT) assumes that the $Na^+$ core is spherically symmetric and frozen in place. So the effective potential, $V_{Na}$ seen by the valence electron is spherically symmetric and only depends on $r$. This potential is lower than the coulomb -1/$r$ potential only at small $r$, and the effect is to increase electron kinetic energy and decrease the wavelength of the radial oscillations relative to H. Suppose the phase shift is $\tau$. The bound state radial wavefunctions are given by:

$$\rho(r) = f(W,l,r)cos\tau - g(W,l,r)sin\tau \tag{3.4}$$

where $f(W,l,r)$ and $g(W,l,r)$ are commonly termed the regular and irregular coulomb functions. This radial function will derive the the allowed eigen energies:

$$W = -\frac{1}{2(n-\delta_l)^2} \tag{3.5}$$

where $n$ is an integer. Equation (3.5) is the equation used in the simulation to calculate the energies of Rydberg atoms. Table 3.1 gives the $0^{th}$ order approximation of the quantum defect for Rb.

| | $s_{1/2}$ | $p_{1/2}$ | $p_{3/2}$ | $d_{3/2,5/2}$ | $f_{5/2,7/2}$ |
|---|---|---|---|---|---|
| $\delta_l$ | 3.13109 | 2.65456 | 2.64145 | 1.347157 | 0.016312 |

Table 3.1:Quantum defects for low-$\ell$ states of Rb [5].

From Table 3.1 we see, for larger $\ell$, because the electron obit is more like a circle, the defect is smaller. For smaller $\ell$, the defect is larger.

## 3.1.2  Properties of Rydberg Atoms

Table 3.2 summarizes the properties dependent on principal quantum number $n$ of Rydberg atoms [8].

| property | $n$ dependences |
|---|---|
| Binding energy | $n^{-2}$ |
| Energy between adjacent $n$ states | $n^{-3}$ |
| Orbital radius | $n^{2}$ |
| Geometric cross section | $n^{4}$ |
| Dipole moment $<ns|er|np>$ | $n^{2}$ |
| Polarizability | $n^{7}$ |
| Radiative lifetime | $n^{3}$ |
| Fine-structure interval | $n^{-3}$ |

Table 3.2: Properties of Rydberg Atoms.

As introduced in later sections, dipole-dipole interaction between Rydberg atoms is proportional to $n^4$. And the Rydberg electrons are far from cores, which makes the them easy to be affect by external forces. The very long enough lifetime of Rydberg atoms also reduces the threshold of detecting the development of atoms. All these superior properties make them ideal objects for researching dipole-dipole interaction and electron dynamics.

## 3.2 Two-Body Model

### 3.2.1 What Is Two-Body Model

When talking about Dipole-Dipole interaction (which will be introduced in detail in 3.3) between atoms, a simplified two-body model is often used. In this model, we suppose one atom can only be affected by its nearest neighbor. Such an assumption is not very accurate of course, because a nearest neighbor could never block the influence from other atoms. But compared to many-body model, two-body model provides a concise way of thinking dipole-dipole interaction between atoms [5]. Besides, two-body effect has been accepted widely to be the major effect between atoms [9][10]. So in this dissertation, all the calculation and simulation is the based on the two-body model.
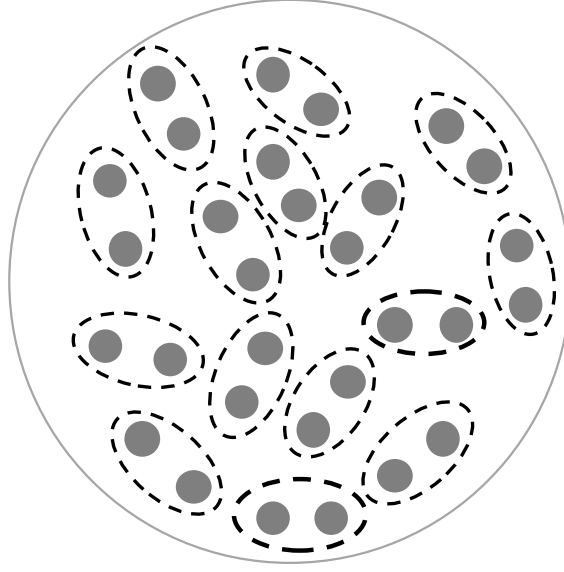
Figure 3.2: Schematic of pairs in MOT. For an atom in a MOT, we only consider the effect from its nearest neighbor. One atom and its nearest neighbor is considered to be "a pair of atoms".

For a two-body model or a pair of atoms, we can write their state, in non-interacting basis, as the combination of their individual states. For example, for a pair of atoms which are in *ns* state and *np* state respectively, we can write the state of this pair as *nsnp*. We call this state "pair state". Such a convention is followed in all sections of this dissertation.

## 3.2.2  Nearest Neighbor Distribution

For a pair of atoms, we need to find the distance between them to get the effect of one atom on the other. We use the so called "Nearest Neighbor Distribution" theory to find the distance between an atom and its nearest neighbor. The nearest neighbor distribution function $H(r)$ for a D-dimensional system is described by [11][12]:

$$H(r) = \rho \frac{dv_D(r)}{dr} \exp\left[-\rho v_D(r)\right] \tag{3.6}$$

where $\rho$ is the density of the atoms and $v_D(r)$ is the volume of the D-dimensional sphere. For a 3-D system, we get the distribution function:

$$H(r) = 4\pi\rho r^2 \exp\left[-\frac{4}{3}\pi\rho r^3\right].\tag{3.7}$$

From Equation (3.7), we can find the most possible distance between in one pair is:

$$R = \sqrt[3]{\frac{1}{2\pi\rho}}.\tag{3.8}$$

For a MOT with density $\rho \approx 10^9$ cm$^{-3}$, temperature about 100 $\mu$K, the most possible distance between one atom and its nearest neighbor is about 5 $\mu$m and the velocity of the atoms is of the order of 10 cm/s. In 1 $\mu$s, one atom can move about 0.1 $\mu$m which is much smaller than the distance between two atoms. So we could consider the atoms as "frozen" or static atoms in the MOT for our experiments.

### 3.2.3  Förster Resonance Energy Transfer

Förster Resonance Energy Transfer (FRET) is a mechanism describing energy transfer between two atoms or molecules. It happens when two neighboring atoms are dipole-dipole coupled to higher and lower states with equal energy spacing. This mechanism could be described very easily using the two-body model (as shown in Figure 3.3). One atom is acting as a donor and the other one accepter. The atoms exchange energy as the donor is de-excited to a lower state and the accepter excited to a higher state. We utilize this mechanism a lot in our research described in this dissertation.
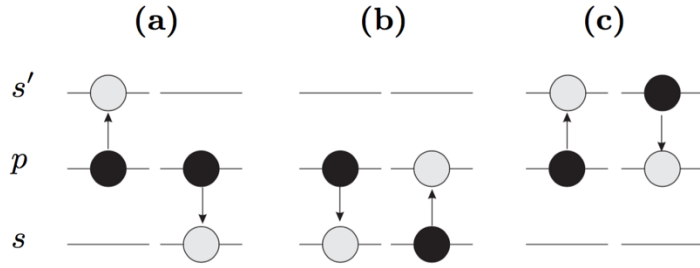
Figure 3.3: Schematic for typical FRETs. Black cycles represent the initial pair states and gray cycles the final pair states. (a) is $pp \rightarrow ss'$, (b) $ps \rightarrow sp$ and (c) $ps' \rightarrow s'p$ [13].

## 3.3 Dipole-Dipole Interaction

In the above discussion, dipole-dipole interaction has been mentioned several times. Now with the Rydberg Atoms model and two-body model, it makes easy to describe what exactly dipole-dipole interaction is.

### 3.3.1 Dipole Moment

For Rydberg atoms, the most external electron spends most of the time far from the positive core. Although the atom as a whole is neutral, it has a polarity. We could simplify a Rydberg atom to be a system composed of a positive charge and a negative charge. Such a system is called a dipole and dipole moment is a measure of the polarity in this system. Its definition expressed in math is:

$$\vec{\mu} = q\vec{r} \tag{3.9}$$

where $q$ is the charges' amplitude and $\vec{r}$ is the vector from the negative charge to the positive charge. This is a classic view of dipole moment and the dipole moment described in Equation (3.9) has a special name "permanent dipole moment". This classic view will

help us to understand the dipole-dipole interaction picture better. But another view from quantum physics is more commonly used.

In quantum physics, dipole moment is expressed as "transition dipole moment" and its definition is associated with the transition between state 1 and state 2:

$$\mu_{12} = \langle 1|r|2 \rangle \tag{3.10}$$

supposing charge is 1. Such a concept is introduced when calculating Schrodinger equation in quantum mechanics (see section 3.3.3). From Equation (3.10) we see if state 1 and state 2 are the same, then the transition dipole moment is 0, which means a transition dipole moment is always an off-diagonal matrix element.

This discussion about dipole moment has been divided into classic view and quantum view. Similar to that, dipole-dipole interaction model will also be explored from both views.

## 3.3.2 Dipole-Dipole Interaction in Classic Picture

Although not very accurate, a classic dipole-dipole interaction picture has useful similarity to the interaction between quantum atoms and helps us to understand the quantum picture.

If there is only one dipole, the potential of this dipole is merely provided by the attractive force between the positive charge and negative charge. When two dipoles are getting close, the potential of such a system will be changed by the dipole-dipole interaction. As shown in Figure 3.4, two dipoles are interacting with each other. The total potential energy of this system does not only contain the inner coulomb potential of each individual dipole but also the potential caused by dipole-dipole interaction. The dipole-dipole interaction potential could be easily written as:

$$V_{dd} = \frac{q^2}{R} - \frac{q^2}{|\vec{r_1} - \vec{R}|} - \frac{q^2}{|\vec{r_2} + \vec{R}|} + \frac{q^2}{|\vec{r_1} - \vec{r_2} - \vec{R}|}. \tag{3.11}$$

From reference [14], Equation (3.11) could be simplified to:

$$V_{dd} = \frac{q\vec{r_1} \cdot q\vec{r_2} - 3(q\vec{r_1} \cdot \hat{R})(q\vec{r_2} \cdot \hat{R})}{R^3}. \tag{3.12}$$

Expressed in dipole moments, Equation (3.12) could also be written as:

$$V_{dd} = \frac{\vec{\mu_1} \cdot \vec{\mu_2} - 3(\vec{\mu_1} \cdot \hat{R})(\vec{\mu_2} \cdot \hat{R})}{R^3} \tag{3.13}$$

where $\vec{\mu_1}$ is the dipole moment of dipole 1 and $\vec{\mu_2}$ is the dipole moment of dipole 2. From this expression, we see that whether the force between the two dipoles is attractive or repulsive is determined by the polarity of their dipole moments.

From Equation (3.13) we can also see the dipole-dipole interaction is strongly affected by the distance between the dipoles or Rydberg atoms. This is the reason why two-body effect is the major effect in an ensemble of frozen atoms.

Suppose $\hat{R} = \hat{z}$ and $q = 1$, Equation (3.12) could also be written as:

$$V_{dd} = \frac{x_1 x_2 + y_1 y_2 - 2z_1 z_2}{R^3} \tag{3.14}$$

where $x_i$, $y_i$, and $z_i$ specify the position of the Rydberg electron in the $i$th atom relative to the center of the atom.
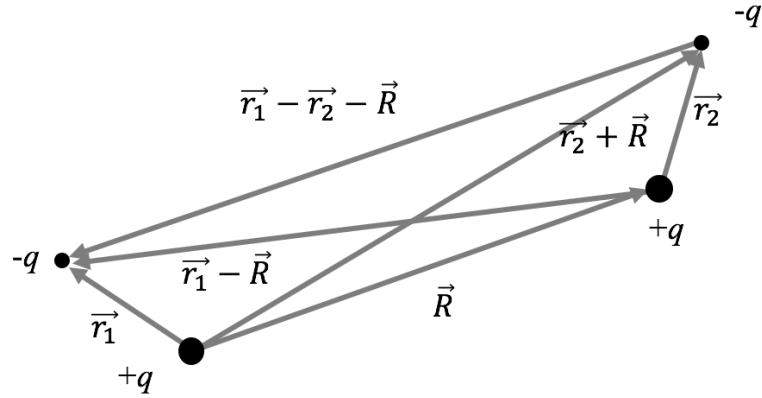
Figure 3.4: Schematic for interaction between two dipoles in classic picture.

### 3.3.3 Dipole-Dipole Interaction in Quantum Picture

The quantum dipole-dipole picture is based on the classic picture. Without loss of generality, we now continue with the resonance (a) in Figure 3.3. Suppose a system is composed of two dipoles starts from pair state *pp*, and we want to explore the evolution of the wavefunction in such a system. So we have:

$$\psi_i = pp, and\ \psi_f = ss'. \tag{3.15}$$

The total Hamiltonian of such a system is $H = H_0 + V$. $V$ is the potential caused by dipole-dipole interaction as we discussion in the classic picture. The solution for time-dependent Schrodinger equation, $H\Psi = i\partial\Psi/\partial t$ is a combination of $\psi_i$ and $\psi_f$:

$$\Psi = C_i(t)\psi_i + C_f(t)\psi_f \tag{3.16}$$

where all of the time dependence is contained in the coefficients $C_i(t)$ and $C_f(t)$. And the Schrodinger equation can be written as:

$$\begin{pmatrix} C_i \\ C_f \end{pmatrix} \begin{pmatrix} E_i & V_{fi} \\ V_{if} & E_f \end{pmatrix} = i \begin{pmatrix} \dot{C}_i \\ \dot{C}_f \end{pmatrix} \tag{3.17}$$

where $V_{pq} = \langle \psi_p | V | \psi_q \rangle$, with $p$ and $q$ representing pair states. And when in resonance

$E_i = E_f = E$. By solving Equation (3.14) we can get two eigen energy values:

$$\begin{cases} E_1 = E + M \\ E_2 = E - M \end{cases} \tag{3.18}$$

where $M$ is expressed as:

$$M = |\langle pp | V | ss' \rangle| \propto |\langle p | r_1 | s \rangle| \cdot |\langle p | r_2 | s' \rangle| = |\mu_{ps} \mu_{ps'}|. \tag{3.19}$$

This expression utilizes the concept of transition dipole moment mentioned in section 3.3.1.

We can also get two eigenstates from Equation (3.14):

$$\begin{cases} \psi_1 = \psi_i + \psi_f \\ \psi_2 = \psi_i - \psi_f \end{cases} \tag{3.20}$$

So the complete solution of the Equation (3.14) is:

$$\Psi = C_1 \psi_1 e^{-iE_1 t} + C_2 \psi_2 e^{-iE_2 t} \tag{3.21}$$

in which $C_1$ and $C_2$ are constants determined by the initial condition.

The above discussion gives us a simple example of dealing with dipole-dipole interactions in a two-state simple system. To calculate the matrix elements for such a system and more complicated systems, we need to go to deeper details. By separating the radial part and the angular part, the calculation is implemented as follows.

From Equation (3.14), using the relations between the Cartesian coordinates and the spherical harmonics ($Y_{lm}$),

$$x = \sqrt{\frac{2\pi}{3}} r(-Y_{11} + Y_{1-1})$$

$$y = i\sqrt{\frac{2\pi}{3}} r(Y_{11} + Y_{1-1})$$ (3.22)

$$z = \sqrt{\frac{4\pi}{3}} rY_{10}$$

the dipole-dipole interaction can be written in terms of spherical harmonics as:

$$V_{dd} = -\frac{r_1 r_2}{R^3} \cdot \frac{4\pi}{3} \cdot ({}^1Y_{11}\,{}^2Y_{1-1} + {}^1Y_{1-1}\,{}^2Y_{11} + 2\,{}^1Y_{10}\,{}^2Y_{10})$$ (3.23)

where ${}^iY_{lm}$ is the spherical harmonics acting on the Rydberg electron of the $i$th atom.

To compute the matrix elements, Edmond's $C$-tensors are introduced [15]. The relation between the spherical harmonic tensors and the $C$-tensors is:

$$C_q^k = \sqrt{\frac{4\pi}{2k+1}} Y_{kq}.$$ (3.24)

So the dipole-dipole interaction in form of $C$-tensors is:

$$V_{dd} = -\frac{r_1 r_2}{R^3} (C_1^1 C_{-1}^1 + C_{-1}^1 C_1^1 + 2C_0^1 C_0^1).$$ (3.25)

In Equation (3.25), a pair of $C$'s implies that the first $C$ acts on the first atom and the second $C$ on the second atoms.

Equation (3.25) is used in the simulation to calculation the matrix elements. As an example, the dipole-dipole matrix element between $p_{1\frac{1}{2}}p_{1\frac{1}{2}}$ and $s_{1\frac{1}{2}}s'_{1\frac{1}{2}}$ is expressed as:

$$\langle p_{1\frac{1}{2}}p_{1\frac{1}{2}}| V_{dd}| s_{1\frac{1}{2}}s'_{1\frac{1}{2}}\rangle = -\frac{r_1 r_2}{R^3}\langle p_{1\frac{1}{2}}|C_0^1|s_{1\frac{1}{2}}\rangle \langle p_{1\frac{1}{2}}|C_0^1|s'_{1\frac{1}{2}}\rangle$$ (3.26)

where $r_1$ and $r_2$ are the radial matrix elements and the single state expression has a format of $\ell_{j\,m_j}$. The radial matrix elements could be calculated using a numerical Numerov integration algorithm [18].

## 3.3.4  Double-Dipole System in Electric Field

In experiments, we utilize THz pulses to redistribute population on different states. The THz electric pulse is essentially an electric field. To simulate the redistribution process, we need to know the model for a double-dipole system in the electric field.

The model is based on the model shown in Figure 3.4. We define the vector pointing from one atom core to the other core to be $z$ axis. The electric field has an angle $\theta$ to the $z$ axis. We define the surface containing the electric field vector and the $z$ axis as the $xz$ surface.
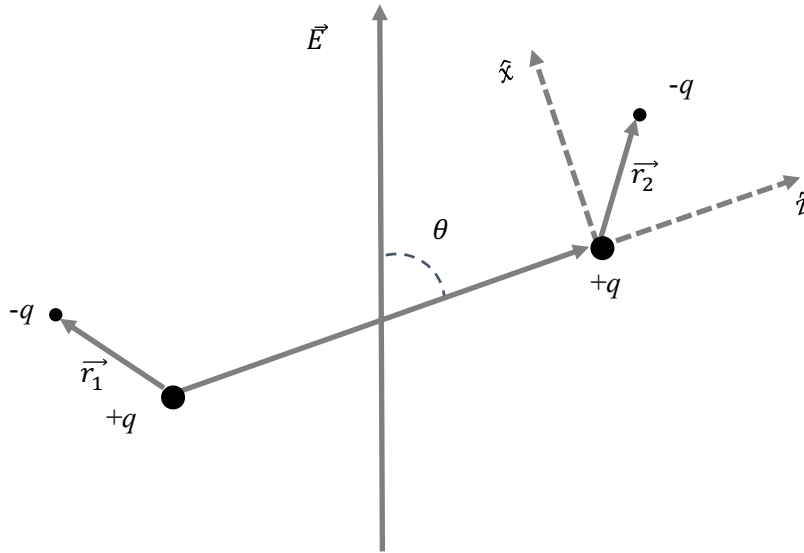
Figure 3.5: Schematic for a double-dipole system in an electric field.

As shown in Figure 3.5, for the electron in atom 1, the effect of the electric field is:

$$H_1 = -q\vec{E} \cdot \vec{r_1} = -qE_0(sin\theta\vec{x_1} + cos\theta\vec{z_1}) \tag{3.27}$$

where $E_0$ is the amplitude of the field, which could be changing over time if the applied

field is a THz pulse.

From Equation (3.22) and (3.24), the above equation could be converted to:

$$H_1 = -q\vec{E} \cdot \vec{r_1} = -qE_0 r_1 (\frac{sin\theta}{\sqrt{2}}(C_1^1 + C_{-1}^1) + cos\theta C_0^1) \tag{3.28}$$

where $\theta$ is not a constant value. For a randomly distributed ensemble composed of many

pairs of atoms, each pair has its own defined $z$ axis thus $\theta$ is different for different pairs.

The total performance is a combination of all the pairs in the ensemble.

Similar rule applies to atom 2. So with an electric filed applied to a double-dipole

system, the Hamiltonian brought by the field is:

$$H_E = H_1 + H_2. \tag{3.29}$$

And we already know the form of dipole-dipole interaction. Using perturbation theory,

we can calculate the evolution of wavepackets in a random ensemble under the influence

of dipole-dipole interaction, as well as the state redistribution when the THz pulses are

applied to the atoms.

## 3.4 Blackbody Radiation Model

Rydberg atoms are strongly affected by blackbody radiation, even at room temperature.

The effect of thermal radiation is due two reasons [5]. First, the energy spacing between

adjacent Rydberg levels are small ($\Delta E \propto n^{-3}$), so that $\Delta E < KT$ at 300K. Second, the

dipole matrix elements of transition between Rydberg states are large, providing coupling

of the atoms to the thermal radiation. Because of the strong coupling between Rydberg

atoms and the thermal radiation, population initially put into one state rapidly diffuse to other energetically nearby states by blackbody radiation.

### 3.4.1 Blackbody Induced Transition

The spontaneous decay rate of the $n\ell$ state to the lower lying $n'\ell'$ state is given by the Einstein $A$ coefficient $A_{n'\ell',n\ell}$ [16]. The thermal radiation induced stimulated emission rate $K_{n'\ell',n\ell}$ is $\bar{n}$, which is the photon occupation number [17], times as large as the spontaneous rate:

$$K_{n'\ell',n\ell} = \bar{n}A_{n'\ell',n\ell} \,. \tag{3.30}$$

In terms of the average oscillator strength, Equation (3.30) is reexpressed as:

$$K_{n'\ell',n\ell} = -2\bar{n}\alpha^3 w_{n'\ell',n\ell}^2 \bar{f}_{n'\ell',n\ell} \tag{3.31}$$

where $\alpha$ is the fine structure constant, $w_{n'\ell',n\ell}$ is the energy difference $W_{n'\ell'} - W_{n\ell}$, and

$$\bar{f}_{n'\ell',n\ell} = \frac{2}{3} w_{n'\ell',n\ell} \frac{\ell_{max}}{2\ell+1} |\langle n'\ell'|r|n\ell\rangle|^2 \tag{3.32}$$

where $\ell_{max}$ is the larger of $\ell$ and $\ell'$.

Equation (3.31) and Equation (3.32) are the equations used in Chapter 4 to calculate the blackbody radiation induced transition rate between nearby Rydberg levels.

### 3.4.2 Radiation Model

When considering the decay of the population in one Rydberg state, as described in Chapter 4, radiation models similar to schematic in Figure 3.6 are used. This is spontaneous decay. There is blackbody induced transition between the starting state and its neighbors.

There is also blackbody radiation between one neighbor and the neighbor's neighbors. And so on.
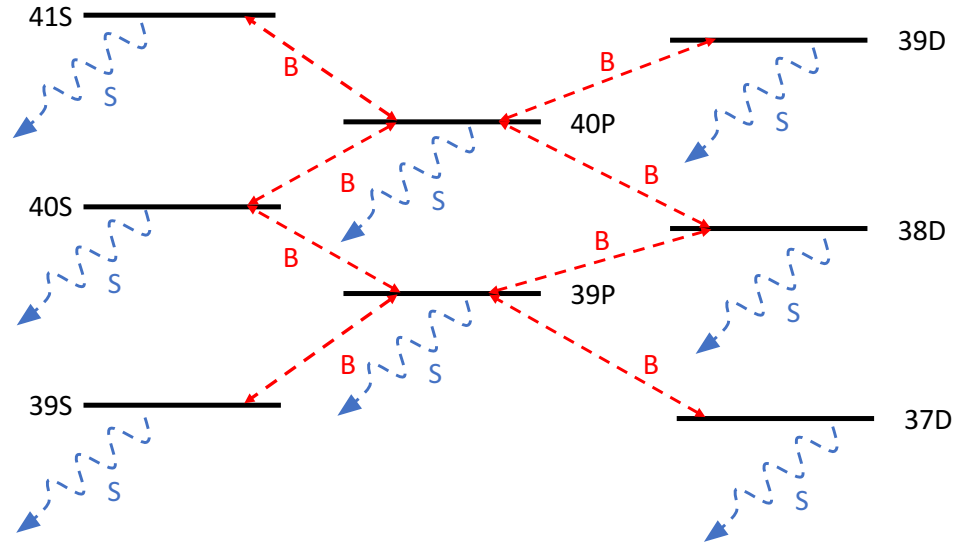


Figure 3.6: Decay model for atoms starting from state 40*s* as an example. The red dash lines between two states mean there is blackbody stimulated transition between these two states. The blue dash curves mean the spontaneous decay.

In reality, there are more states involved in the decay and transition process and the situation is much more complicated. But for calculation convenience, a limited number of nearby states are chosen. To make sure such a simplification is reasonable, results based on different numbers of states are compared to find a proper number of nearby states which shares a very close results from the calculation with more states.

# Bibliography

[1]   H. E. White, Introduction to Atomic Spectra, McGraw-Hill, New York (1934).

[2]   G. D. Living and J. Dewa, Proc, Roy, Soc. Lond, 29, 398 (1879).

[3]   W. N. Hartley, J. Chem. Soc. 43, 390 (1883).

[4]   J. R. Rydberg, Phil. Mag. 5th Ser. 29, 331 (1890).

[5]   Thomas F. Gallagher. Rydberg Atoms. Cambridge University Press (1994).

[6]   R. Shankar, Principles of Quantum Mechanics, 2nd Edition, Plenum Press (1994).

[7]   M. J. Seaton, Rep. Prog. Phys. 46, 167 (1983).

[8]   Thomas F. Gallagher. Rep. Prog. Phys. 51, 143 (1988).

[9]   B. Sun and F. Robicheaux, Spectral Linewidth Broadening from Pair Fluctuations in A Frozen Rydberg Gas, Phys. Rev. A. 78, 040701 (2008).

[10]  I. Mourachko, D. Comparat, F. de Tomasi, A. Fioretti, P. Nosbaum, V. M. Akulin, and P. Pillet, Many-Body Effects in a Frozen Rydberg Gas, Phys. Rev. Lett. 80, 253 (1998).

[11]  S Torquato, B Lu and J Rubinstein, Nearest-neighbour Distribution Function for Systems of Interacting Particles, J. Phys. A: Math. Gen. 23 (1990)

[12]  Hertz P, Math. Ann. 67 387 (1909).

[13]  S. Westermann, T. Amthor, A.L. de Oliveira, J. Deiglmayr, M. Reetz-Lamour, and M. Weidemuller, Dynamics of resonant energy transfer in a cold Rydberg gas, Eur. Phys. J. D 40, 37–43 (2006).

[14]  F. Robicheaux, J. V. Hernández, T. Topçu,1 and L. D. Noordam, Simulation of Coherent Interactions between Rydberg Atoms, Phys. Rev. A. 70, 042703 (2004).

[15]  A. R. Edmonds, Angular Momentum in Quantum Mechanics, Princeton University Press, Princeton (1960).

[16]  H. A. Bethe and E. A. Salpeter, Quantum Mechanics of One-and-Two-Electron Atoms, Academic Press, New York (1957).

[17]  R. Loudon, The quantum Theory of Light, Oxford University Press, London (1973).

[18]  M. L. Zimmerman, M. G. Littman, M. M. Kash, and D. Kleppner, Rydberg States of Atoms and Molecules, Phys. Rev. A 20, 2251 (1979).

# 4 Absence of Collective Decay in a Cold Rydberg Gas

We have studied the decay of Rydberg excitations in a cold Rb gas. A 10 ns, pulsed-dye-amplified diode laser excites Rb atoms at 70 $\mu$K in a magneto-optical trap to *ns* or *np* Rydberg states with principal quantum numbers $26 \leq n \leq 40$. Time-delayed state-selective field ionization is used to directly monitor the population in the initial and neighboring Rydberg levels. The measured time dependence of the Rydberg population is well described by numerical simulations which consider only spontaneous emission and population transfer by blackbody radiation. No evidence for collective decay is found at atom densities up to $3 \times 10^9 \text{cm}^{-3}$. This result is in contrast to a previous study [Wang *et al.*, Phys. Rev. A **75**, 033802 (2007)], in which superradiant decay was theoretically predicted and experimentally inferred for atom density and laser focal volume conditions very similar to those considered here. Suppression of collective emission is likely due to variations in transition energies within the atom sample, dominated by inhomogeneities in dipole-dipole exchange interactions for initial *s* states, or by a combination of dipole-dipole and electric field inhomogeneities for the initial *p* states.

# 4.1 Introduction

Atoms within cold Rydberg ensembles are coupled by strong long-range dipole-dipole (DD) interactions [1], making them interesting systems for exploring few- and many-body quantum dynamics in general and applications in quantum information in particular [2–35] (The properties of Rydberg Atoms are described in Chapter 3). Of course, unlike in ground-state systems, finite Rydberg lifetimes limit the types of measurements and number of coherent manipulations that can be performed in a given experiment. Fortunately, isolated Rydberg atoms exhibit low spontaneous decay rates [1], potentially enabling processing over micro- to millisecond time scales. At first glance this stability against radiative decay might seem surprising given the large transition matrix elements between adjacent Rydberg states, which scale as $n^2$. However, spontaneous decay to nearby levels via low-frequency emission is strongly suppressed by the $\omega^3$ dependence of the Einstein *A* coefficient. As a result, the predominant decay path for isolated Rydberg atoms in low-angular-momentum states is to the ground or low-lying excited levels, resulting in an $n^{-3}$ scaling of the spontaneous emission rate.

That said, neighboring Rydberg levels can play a dominant role in the decay of a large number $N$ of atoms which either are simultaneously excited in a volume with dimensions smaller than the wavelength λ of the emitted light, or are sequentially excited throughout a cylindrical volume with length $L \gg \lambda$ [36,37]. In his seminal paper [38], Dicke predicted that a dense collection of $N$ radiators, either in very close proximity or in a properly phased extended distribution, could develop spontaneous correlations and collectively emit radiation at rates greatly exceeding ("superradiance"), or much smaller than ("subradiance"), those of individuals in the sample. For the two-level systems considered by Dicke, correlations between a large number of emitting atoms can initiate collective superradiant emission at a per atom rate up to *N/4* times larger than that between the same

two levels in an isolated atom [38]. Collective emission remains a subject of considerable interest in many different contexts, including Rydberg atoms [39–51].

The presence of blackbody radiation, the existence of multiple photo decay channels in a Rydberg ladder, and strong DD interactions between atoms, all explicitly neglected in Dicke's original paper (and in many subsequent treatments) [38,52,53], make it much more difficult to observe, characterize, and quantitatively predict collective decay phenomena in Rydberg gases. In particular, DD interactions can suppress superradiance. In a thermal gas, this suppression results from DD-mediated collisions that homogeneously dephase the individual emitters in the ensemble at a rate greater than the superradiance rate [50]. In a frozen gas, DD exchange interactions couple pairs, or larger groups, of atoms leading to a variation in transition energies across the ensemble. Such inhomogeneities squelch the correlations that underlie superradiance, along with the collective emission [47]. That said, a clear signature of superradiance between Rydberg states, a fluorescence cascade from a Rydberg ladder proceeding at a rate much greater than spontaneous emission of isolated atoms, was first observed following pulsed-laser excitation of an elongated volume ($L \gg \lambda$) in a thermal cell [36]. More recently, direct evidence for superradiance was found in the millimeter-wave emission from a large cylindrical volume of Ca Rydberg atoms in a supersonic expansion, also with $L \gg \lambda$ [49,50]. As pointed out in the latter work, the rates for superradiant decay and DD dephasing within a given decay channel are essentially identical, up to a multiplicative geometric factor $L/\lambda$ in the superradiance rate formula. Accordingly, it was suggested that collective decay should not play a major role in Rydberg depopulation unless $L \gg \lambda$ [50].

Still, despite competing DD effects, under certain conditions superradiance should play some role in cold ensembles where the dimensions of the excited volume are less than or comparable to $\lambda$. Indeed, evidence of reduced Rydberg lifetimes has been reported in several such experiments [39,48,51,54,55]. For example, Feng et al. observed a density-

dependent lifetime suppression of Cs Rydberg atoms in a magneto-optical trap (MOT) [54]. They attribute the suppression to a combination of neutral Rydberg atom collisions and superradiance. However, the evidence for superradiance appears tenuous as their calculations with and without superradiant contributions both fall within their measurement uncertainty (see their Fig. 2). In addition, if one applies their values for Rydberg collision velocity and cross section, the collisional depopulation rates are over three orders of magnitude too small to account for their observations. Han and Maeda attributed population transfer from initial to neighboring Rb Rydberg states to superradiance, but provided no evidence ruling out other possible population transfer mechanisms [56]. In other measurements, using fluorescence detection, Day et al. found Rydberg depopulation rates that were roughly twice that expected from single-atom spontaneous emission over a range of $n$ states and at low densities, $\rho \sim 1 \times 10^7$ cm$^{-3}$ [48]. The small variation of the lifetime suppression with principal quantum number coupled with trap loss measurements argued against collisional depopulation and blackbody ionization. Instead, the enhanced Rydberg decay rate was found to be qualitatively consistent with a simplified collective decay model. In other experiments, the inclusion of superradiant decay channels was found to improve the quality of model fits to electromagnetically induced transparency measurements in cold Rydberg gases [51,55].

Certainly, a substantial decrease in Rydberg lifetimes due to collective emission would have a significant impact on most cold Rydberg atom experiments. Perhaps more important, in the context of the exploration and control of few- or many-body Rydberg dynamics, are the influences of the spontaneous quantum correlations that are predicted to develop with the emission of the first photon from the sample and evolve as the Rydberg population descends through a ladder of Dicke states [38,53]. Interestingly, Wang et al. presented a sophisticated theoretical treatment of photo decay in a multilevel Rydberg system which makes definite predictions as to whether superradiance should occur for a given initial

principal quantum number, atom density, and experimental volume [39]. The theory apparently reproduced the rapid decay, at a rate approximately 40 times greater than predicted from spontaneous emission alone, of an initial population of $43p$ atoms in a MOT at a density of $\rho \sim 5 \times 10^8$ cm$^{-3}$.

We have used pulsed-laser excitation of Rb Rydberg atoms in a MOT under conditions ostensibly similar to those used in Ref. [39] in an attempt to test the predictions of their Rydberg superradiance theory. We employ state-selective field ionization (SSFI) to measure the population in the initial and neighboring Rydberg states as a function of delay after the laser excitation. We find no evidence for the predicted collective decay over a range of principal quantum numbers $26 \leq n \leq 40$, and atom densities $\rho \sim 3 \times 10^9$ cm$^{-3}$, despite the fact that, for these states, our highest density is more than two orders of magnitude above the predicted superradiance threshold [39]. Instead, our measurements are consistent with noncorrelated spontaneous decay combined with population redistribution via blackbody radiation.

## 4.2 Experimental Procedure and Results

General information about the setup could be found in Chapter 2. This section provides some particular information about the experiment approach.

In the experiments, $^{85}Rb$ atoms at 70 $\mu$K are held in a MOT. The full width at half maximum (FWHM) diameter of the atom cloud is 0.4 mm. The MOT is positioned at the center of four parallel rods which facilitate the application of static and pulsed electric fields in the y direction for exciting and detecting Rydberg atoms in the MOT. A 10 ns pulsed, tunable, dye-amplified, ~480 nm diode laser propagating in the x direction is focused into the center of the MOT, creating a cylindrically shaped volume of cold Rydberg atoms with a FWHM diameter of ~0.1 mm and a length of 0.4 mm. The MOT and Rydberg lasers are

non collinear, preventing the excitation of Rydberg atoms throughout any extended volume from the lower-density background of thermal Rb atoms in the chamber. The ~100 MHz bandwidth of the Rydberg excitation laser ensures that there is no excitation suppression via dipole blockade [2,3]. At a variable time $\tau$ after the laser excitation, a ramped voltage is applied to two of the rods, ionizing any Rydberg atoms in the interaction region and pushing the resulting ions toward a micro channel plate (MCP) detector. Ions originating from different Rydberg states arrive at the detector at different times. The integrated signals in different time bins are proportional to the populations in different Rydberg states and are recorded for each laser shot as a function of the ionization time $\tau$. The experiment proceeds at the 15 Hz dye-laser repetition rate.

The diode laser is tuned to selectively excite atoms from the upper $5p$ trap level to $ns$ and $np$ Rydberg states with $26 \leq n \leq 40$. Excitation of $np$ states is facilitated by the application of a weak static electric field (from 30 V/cm 177 at $n=26$, 16 V/cm at $n=32$, to 7 V/cm at $n=40$). By saturating the Rydberg excitation using high laser fluence, we ensure that 50% of the $5p$ atoms within the interaction volume are excited to Rydberg states, enabling us to determine the Rydberg atom density [57]. Subsidiary experiments on resonant energy transfer between Rydberg atoms are consistent with the Rydberg density determination [57,58]. The MOT fluorescence is monitored throughout the lifetime measurements, ensuring that the number of atoms in the MOT is constant to within a few percent as $\tau$ is scanned. Care is taken to minimize the amplified spontaneous emission from the dye-amplified laser pulse, eliminating direct photoionization of $5p$ atoms. For the $s$-state measurements, a small, ~1.5 V/cm, residual electric field persists in the interaction region due to imperfect shielding of the high voltage biased MCP (a larger field is present for initial $p$ states). This field is sufficient to eject any ions or electrons from the interaction region, eliminating extended interactions between charged particles and neutral Rydberg atoms, and preventing the spontaneous evolution of the Rydberg gas into a plasma [59,60].

Neither the small static field employed for the *p*-state measurements nor the smaller residual field present during the *s*-state measurements substantially alters the rates for spontaneous emission or population transfer induced by blackbody radiation. The potential influence of the field inhomogeneity on superradiant decay is considered in the Analysis and Discussion section below.

Figure 4.1 and Figure 4.2 show our principal experimental results. In Figure 4.1 (a) and (c), the probabilities for finding atoms in the 26*s* + 25*p*, 32*s*, and 40*s* states are plotted as functions of detection time $\tau$ for the maximum densities explored, $\rho \sim 3 \times 10^9$ cm$^{-3}$ and $\rho \sim 1.5 \times 10^9$ cm$^{-3}$, respectively. Note that for the lowest initial *n* state the sum of the 26*s* and 25*p* populations is shown since their corresponding features could not be adequately separated in the time-resolved field-ionization signal. Within experimental uncertainties, the decays for the three initial *s* states are identical at the two densities shown. Additional measurements were made at Rydberg densities as low as $\rho \sim 2 \times 10^8$ cm$^{-3}$ (for 32*s* initial states) and $\rho \sim 5 \times 10^8$ cm$^{-3}$ (for 32*p* initial states), but no statistically significant differences were observed in the decays.

For spontaneous decay of isolated atoms at absolute zero, one would expect lifetimes of 28 and 58 $\mu$s for the 32*s* and 40*s* atoms, respectively [61]. The measured lifetimes for the 32*s* and 40*s* states are substantially smaller, 19 and 38 $\mu$s, respectively, due to population redistribution by blackbody radiation from the 300 K environment surrounding the MOT. Indeed, redistributed population is detected in neighboring Rydberg levels. In particular, Figure 4.1 (b) and (d) show the delay-dependent population in the *p* states (26*p*, 32*p*, and 40*p*) that lie immediately above the respective initial s states. Although we would expect to find some atoms in the adjacent, lower-lying *p* states as well, small features reflecting that population in the time-of-ionization signal lie within the initial-state peak (for the case of 26*s*) or are masked by the tail of the larger, initial-state peak which precedes it.

Figure 4.1: (a), (c) Probabilities for finding atoms in 26*s* + 25*p* (green, fastest decay), 32*s* (red, intermediate decay), and 40*s* (blue, slowest decay) as a function of detection time $\tau$ for Rydberg densities of $\rho \sim 3 \times 10^9$ cm$^{-3}$ (a) and $\rho \sim 1.5 \times 10^8$ cm$^{-3}$ (c). Note that the sum of the 26*s* and 25*p* populations is shown since their corresponding features could not be adequately separated in the field-ionization signal. Vertical bars show the experimental data with uncertainties, and the solid curves are calculated as described in the text. Measurements and calculations for the 40*s* decay extend to 500 $\mu$s where the remaining population is negligible. (b), (d) Probabilities for finding atoms in 26*p* (green, fastest rise and decay), 32*p* (red, intermediate rise and decay), and 40*p* (blue, slowest rise and decay) levels as a function of detection time $\tau$. The states are populated by blackbody redistribution from the initial 26*s*, 32*s*, and 40*s* levels, respectively. The data were measured simultaneously with those shown in (a) and (c). Vertical bars show the experimental data with uncertainties, and the solid curves are calculated as described in the text. The measured *p*-state probabilities are normalized to the calculations as described in the text. The calculations have no free parameters and consider only the effects of spontaneous emission and blackbody radiation on isolated atoms.

The measured lifetime for the combined $26s + 25p$ states is 14 $\mu$s, the same as that expected from spontaneous decay of the $26s$ level alone [61]. Simulations (described in detail below) indicate that this apparent agreement is not due to the absence of blackbody transfer out of $26s$. Rather, the small longer-lived $25p$ component of the signal masks much of the change in the $26s$ decay, with a predicted effective lifetime of 13 $\mu$s for the $26s + 25p$ combination, similar to what we observe. We note that due to the slow rate of the ionizing field, there is a distribution of ionization times and, therefore, of detection efficiencies for atoms in different states. As a result, each of the measured $p$-state populations in Figure 4.1 (b) and (d) has been multiplied by a normalization factor to obtain the best agreement with the calculated decay curves that are shown in the figures and described in the next section.

Figure 4.2 shows analogous data for the decay of initially excited $26p$, $32p$, and $40p$ states. Again, due to blackbody redistribution, the lifetimes associated with these decays (18, 31, and 51 $\mu$s), are considerably smaller than expected from spontaneous emission alone (37, 75, and 155 $\mu$s) [61]. However, in this case, no substantial population is detected in the neighboring $s$ or $d$ levels. The analysis described in the next section indicates that the populations in these states are not detectable within our signal-to-noise ratio, remaining at or below the few percent level due to the relatively rapid spontaneous emission rate out of the s states, and smaller $p \rightarrow s$ and $p \rightarrow d$ blackbody transition rates.
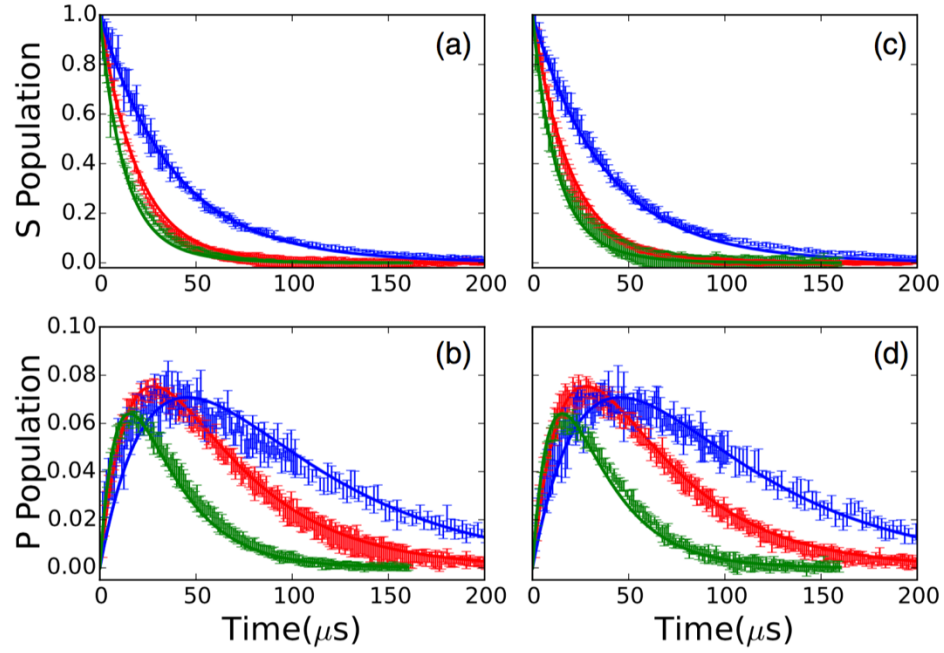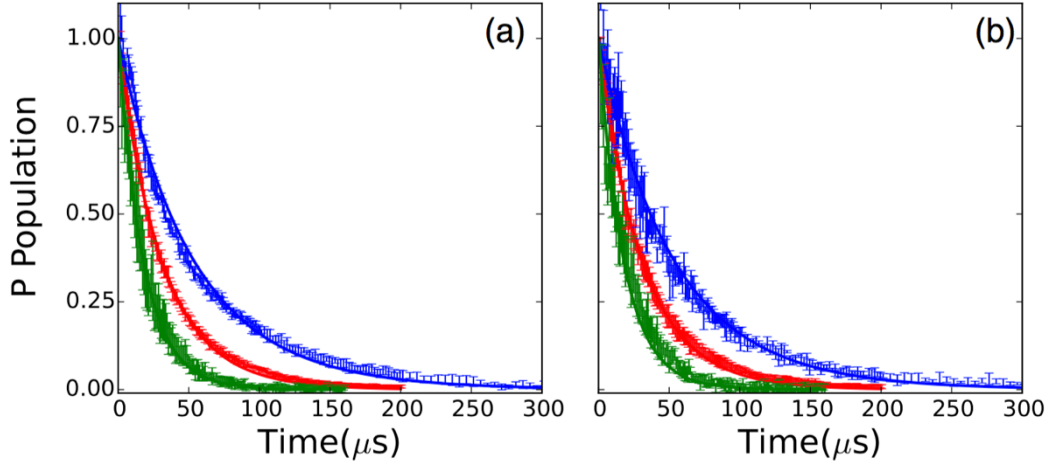
Figure 4.2: Probabilities for finding atoms in 26$p$ (green, fastest decay), 32$p$ (red, intermediate decay), and 40$p$ (blue, slowest decay) as functions of detection time $\tau$ for Rydberg densities of $\rho\sim 3\times 10^9$ cm$^{-3}$ (a) and $\rho\sim 1.5\times 10^9$ cm$^{-3}$ (b). Vertical bars show the experimental data with uncertainties, and the solid curves are calculated as described in the text. Measurements and calculations for the 40$p$ decay extend to 500 $\mu$s where the remaining population is negligible. The calculations have no free parameters and consider only the effects of spontaneous emission and blackbody radiation on isolated atoms.

## 4.3 Analysis and Discussion

To determine if collective processes play any significant role in the decays we observe, we compare the measurements to the results of a simple rate equation model which has an example schematic shown in Figure 3.6. The model includes population transfer via stimulated emission and absorption of blackbody radiation between an essential set of $s$, $p$, and $d$ Rydberg states neighboring the initial level, as well as spontaneous emission out of those essential states to (undetected) lower-lying levels. We calculate the blackbody transition rates between the essential states [1] as well as the known total spontaneous emission rates of the $s$, $p$, and $d$ Rydberg levels.

For example, for an initially excited $40s$ state, the rate equation describing the time-dependent population in the initial $40s$ level is:

$$\frac{dN_{40s}}{dt} = \left(-A_{40s} - B_{40s \rightarrow 40p} - B_{40s \rightarrow 39p}\right)N_{40s} + B_{39p \rightarrow 40s}N_{39p} + B_{40p \rightarrow 40s}N_{40p} \tag{4.1}$$

where $N_{n\ell}$ is the population in state $n\ell$, $A_{40s}$ is the $40s$ spontaneous decay rate, and $B_{n\ell \rightarrow n'\ell'}$ is the blackbody transition rate from $n\ell$ to $n'\ell'$:

$$B_{n'\ell',n\ell} = -2\bar{n}\alpha^3 w^2_{n'\ell',n\ell}\bar{f}_{n'\ell',n\ell} \tag{4.2}$$

which is mentioned in Chapter 3.

The populations in the secondary states $39p$ and $40p$ are computed using similar rate equations that include the total spontaneous decay rate out of those levels as well as blackbody transitions to and from pairs of $s$ and $d$ levels that lie immediately above and below each $p$ state. We truncate the system of equations with rate equations that include spontaneous decay from the tertiary $s$ and $d$ levels and their blackbody couplings with the secondary states. Analogous systems of equations are used to compute the Rydberg population decay following initial $p$-state excitation. We note that, for initial or intermediate $p$ states in particular, blackbody radiation redistributes a small, but non-negligible, fraction of the initial population beyond the nearest-neighbor $s$ and $d$ states. Therefore, an approximate expression

$$B_{n\ell} = \frac{4\alpha^3 kT}{3n^2} \tag{4.3}$$

for the total blackbody decay rate from each $p$ level is used to more accurately account for the net transfer out of these states.

The results of our calculation, which ignore any collective decay phenomena, are shown with the data in Figure 4.1. Overall, the agreement is reasonable. Aside from the previously noted renormalization of the experimental $p$-state population, no parameter

adjustments have been made to obtain the level of agreement shown. The data provides no evidence of a significant reduction in the Rydberg lifetimes due to superradiance. This is true over a range of principal quantum numbers and atom densities where superradiant emission has been predicted to be the dominant decay path [39].

It is well established that superradiance is suppressed by inhomogeneities in transition energies across a sample of emitters [47], and we suspect that this is the case in our, and many other, cold atom experiments. In our experiments, three different effects contribute to such inhomogeneities. The first, and dominant mechanism for some of our measurements, is the DD exchange interaction. Consider a pair of identical atoms with two levels *s* and *p* and interatomic separation *R*. Spontaneous emission from the initial upper pair state *ss* results in the population of the bright configuration of the lower-energy pair state (*sp* + *ps*)/$\sqrt{2}$. However, due to the DD coupling between the atoms, $V_{DD} \propto |\langle s|r|p\rangle|^2/R^3$, the energy of this state is not the same as that for two atoms at infinite separation [1]. Accordingly, in a large ensemble of randomly spaced atoms, every possible configuration of $N_s$ *s* atoms and $N_p$ *p* atoms has a different energy, depending on the separation (and relative orientation) between the *p* atoms and their neighboring *s* atoms. As a result, any Dicke state, the bright linear combination of all possible configurations of $N_s$ *s* atoms and $N_p$ *p* atoms [38], is nonstationary. The phases of the constituent *N*-atom product states evolve at different rates, as determined by their DD energy shifts relative to their energies at infinite separation. The emission from these nonstationary Dicke states dephases at a rate comparable to the typical dipole-dipole energy shift $V_{DD}$ for pairs of atoms in the ensemble. Superradiance cannot occur unless the system transitions down each step in the Dicke ladder more rapidly than this dephasing. A similar argument has been made by Gross and Haroche [62]. In the frequency domain, atoms with different transition energies at different locations in the ensemble do not collectively emit into the same field unless that emission occurs in a very short burst with a sufficiently broad, coherent bandwidth.

To determine the DD dephasing rate, we use the most probable nearest-neighbor separation in a random ensemble as we mentioned in 3.2.2, $R \simeq (2\pi\rho)^{-3}$, and average over all orientations of the Rydberg states on any two neighboring atoms $ns$ and $n'p$ to obtain [63,64]:

$$\overline{V_{\mathrm{DD}}} = \frac{8\pi}{9}\rho |<ns|r|n'p>|^2 \tag{4.4}$$

Using a numerical Numerov integration algorithm to compute the relevant radial matrix elements [65], at the highest density studied ($\rho = 3 \times 10^9\ cm^{-3}$) we obtain values for the DD exchange coupling between the ns and $(n-1)p$ states, $\overline{V_{DD}}$= 2.4, 6.2, and 17 MHz, for $n = 26$, 32, and 40, respectively. These interaction strengths set effective lower limits for the rates at which collective emission from $ns$ to $(n-1)p$ can occur. Similarly, for initial $np$ states and $\rho = 3 \times 10^9\ cm^{-3}$, the relevant exchange coupling is to the nearest lower-lying $s$ states, with , $\overline{V_{DD}}$= 3.1, 7.8, and 20 MHz, for $n = 26$, 32, and 40, respectively.

The magnetic field gradient in the MOT is another source of energy inhomogeneities in our ensemble. As in Ref. [39], the magnetic field remains on during our measurements, resulting in a transition energy variation of approximately 1 MHz across the MOT. This inhomogeneity is smaller, or much smaller, than that due to dipole-dipole interactions at sufficiently high densities. It should not play a principal role in suppressing superradiance under the conditions used to produce Figure 4.1 and Figure 4.2.

The third contributor to the Rydberg energy variations across the ensemble is electric field inhomogeneity. While the voltages applied to the field rods produce a field that is quite uniform over the MOT (predicted field variations of 0.07%, corresponding to 21 mV/cm for the largest applied field of 30 V/cm for the 26$p$ measurements) the residual field from the MCP is not as uniform. Using a combination of spectroscopic measurements and accurate Stark energy calculations, we determine an upper limit for the Rydberg energy inhomogeneity due to the nonuniformity of the electric field $F$ in the interaction region.

First, we measure the transition frequencies for excitation of $32p_{3/2}$ $|m_j| = 1/2,3/2$, from

the $5p_{3/2}$ upper trap state as a function of the voltage applied to the field rods (see Figure

4.3). For convenience, in the following discussion we refer to the field produced by the

rods as the "applied" field. The experimental geometry is identical to that used for the

lifetime measurements, but the Rydberg excitation is performed with an unamplified, 3 $\mu$s

pulse chopped from the ~1 MHz bandwidth cw diode laser. The Rydberg excitation pulse

has ~1 $\mu$s rise and fall times and is formed using an acousto-optic modulator. We use a

temperature- and pressure-stabilized Fabry-Pérot interferometer to track the relative

frequency of the Rydberg laser as it is scanned. The population in $|m_j| = 1/2$ is distinguished

from that in $|m_j| = 3/2$ using SSFI. By recording the signal in two different time bins we

obtain (nominally) separate excitation profiles to the two $|m_j|$ states in the same laser

frequency scan. Therefore, the energy splitting between the two $m_j$ states can be accurately

determined to well within the excitation bandwidth which is dominated by the 6.07 MHz

natural linewidth of the initial $5p_{3/2}$ level.

In zero electric field, the excitation profiles associated with the population in the two

$|m_j|$ levels should exhibit maxima at the same laser frequency, i.e., have zero energy

splitting. However, as shown in Figure 4.4, we observe a minimum splitting of 2 MHz at

an applied field of −2.8 V/cm. The minimum splitting at nonzero applied field allows us to

determine the components of the MCP field parallel and perpendicular to applied field.

Apparently, the application of a −2.8 V/cm rod field minimizes the net field in the

interaction region. Accordingly, there must be a parallel, 2.8 V/cm, MCP field component

which we call the "offset" field. Using the variation in the $|m_j|$ splitting as a function of

applied field, we can also extract a value, 1.5 V/cm, for the perpendicular, i.e., "residual,"

MCP field component. The solid curve shown with the data in Figure 4.4 is the predicted

$32p_{3/2}$ $|m_j| = 1/2,3/2$ splitting as a function of applied field (extracted from a full numerical

Stark map calculation based on the method of Zimmerman et al. [65]), assuming MCP offset and residual fields of 2.8 and 1.5 V/cm, respectively. The good agreement with experiment confirms the accuracy of the calculation as well as the offset and residual field determinations.

At, and near, the minimum splitting (i.e., in the presence of the residual field alone where the *s*-state decay measurements are performed), the $|m_j|$ excitation resonances have minimum linewidths of 8 MHz (see Figure 4.3). As noted above, the predominant contribution to this linewidth is the 6.07 MHz natural width of the $5p_{3/2}$ level. However, the laser bandwidth, Zeeman shifts due to magnetic field inhomogeneities, and Stark shifts due to inhomogeneities in the 1.5 V/cm residual field also contribute. Assuming that the laser spectrum and field distributions are Gaussian, we deconvolute the primary line shape as a Voigt profile, and extract a bandwidth of 3.9 MHz for the total Gaussian contribution. Accordingly, we obtain an upper-limit estimate for the electric field inhomogeneity by assuming it is the sole contributor to this width. From the Stark shift of the $32p_{3/2}$ $m_j = 1/2$ level, $E = 6.5$ MHz/(V/cm)$^2$ $F^2$, we determine that the maximum possible variation of the residual field across the interaction region is $F_{res} = 0.20$ V/cm. Using this field inhomogeneity with the field-dependent Stark shifts of the respective levels, we can compute the maximum range of transition energies between the initial *s* states and the *p* states immediately below them (to which the dipole coupling is the strongest). For the 26*s* $\rightarrow$ 25*p*, 32*s* $\rightarrow$ 31*p*, and 40*s* $\rightarrow$ 39*p* transitions, the maximum energy variations across the excitation region (with only the residual field present) are 0.43, 2.2, and 12 MHz, respectively. The transition energy variations are smaller for transitions to lower lying *p* states due to the $n^7$ scaling of the Rydberg polarizability. So, at the highest densities we have explored, the energy inhomogeneities associated with the residual electric field are less, or much less, than those associated with the dipole-dipole exchange interaction.

Therefore, the electric field inhomogeneities do not hold the primary responsibility for the suppression of superradiance from any of the initial $s$ states.
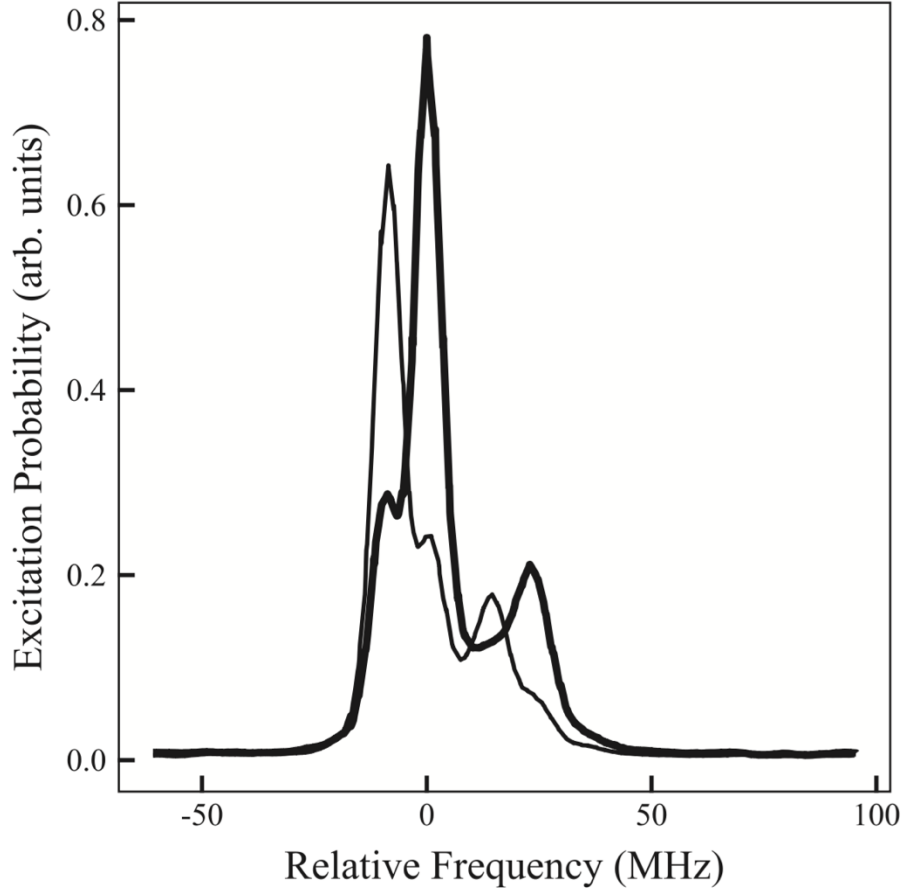


Figure 4.3: Measured $32p_{3/2}$ $|m_j| = 1/2$ (bold line) and $|m_j| = 3/2$ (thin line) excitation probabilities as a function of Rydberg laser frequency in zero applied field. The two data curves are obtained simultaneously in the same laser frequency scan. The small feature on the left (right) of the main $|m_j| = 1/2$ (3/2) peak is the result of imperfect discrimination of the $|m_j| - 1/2$ and 3/2 components via SSFI. The additional peak on the right of the main feature in each trace is due to the trap-laser dressing of the $5p_{3/2}$ and $5s$ levels. Its frequency shift from the main peak reflects the Autler-Townes splitting of the $5p_{3/2}$ initial state.
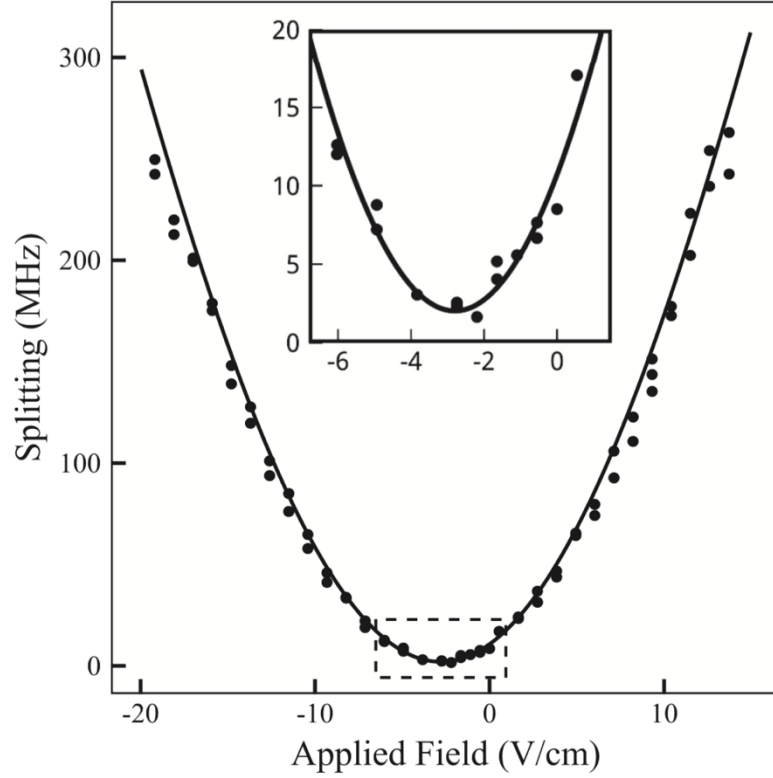
Figure 4.4: Difference (i.e., splitting) in the transition energies for exciting $32p_{3/2}$ $|m_j|=$ 1/2,3/2 from $5p_{3/2}$ as a function of applied electric field. Filled circles are measurements and the solid curve is the result of a numerical Stark map calculation assuming orthogonal "offset" and "residual" electric field components due to the MCP of 2.8 and 1.5 V/cm, respectively. The inset shows a magnified view of the portion of the main figure within the dashed window.

The situation with the initial $p$ states is somewhat different, as they are excited in a nonzero applied field that is considerably larger than the orthogonal residual field. As a result, the residual field and its inhomogeneity have essentially no effect on the transition energies. However, the spatial variations in the MCP offset field, which is parallel to the applied field, cannot be neglected. We use measurements of DD-mediated resonant energy transfer between Rydberg atoms to obtain an upper-limit estimate for the offset field

inhomogeneity. Those experiments use the same experimental geometry as the Rydberg

decay measurements [58,64]. In the experiments, the probability for resonant population

transfer from one pair of Rydberg states to another (e.g., 25*s* + 33*s* → 24*p* + 34*p* [64]) is

recorded as a function of an applied field which Stark-tunes the total energies of the atom

pair in the two different configurations. In a uniform field, the line shape describing the

field-dependent energy transfer probability is characterized by a peak at the "resonance"

condition, where the total energies of the two sets of atom pair states are identical, and a

width that is proportional to the Rydberg density. In a nonuniform field, the line shape has

a nonzero minimum width as the density approaches zero, due to variations in the local

field at different locations within the sample. Consider the 25*s* + 33*s* → 24*p* + 34*p*

resonance [64] for which maximum population transfer occurs in an electric field of *F* ~

3.4 V/cm. Assuming that the nonzero resonance width that is observed at very low Rydberg

density [64] is due solely to the inhomogeneity in the electric field (i.e., ignoring magnetic

field inhomogeneities and any other broadening effects) we obtain the maximum possible

variation in the offset field, $F_{off}$ = 0.08 V/cm, across the Rydberg sample. As an additional

check, we consider a different energy transfer resonance, 32*p* + 32*p* → 33*s* + 32*s*, that is

centered at a substantially higher field *F* ~ 11.5 V/cm [58]. The nonzero low-density width

for this energy transfer resonance gives the same maximum value for the offset field

inhomogeneity, $F_{off}$ = 0.08 V/cm.

Given $F_{off}$, we can compute the maximum possible variations in the energies,

associated with transitions between initial *p* states and the nearest lower-lying *s* state, due

to the inhomogeneous field. Using $F_{off}$, the calculated Stark shifts of each of the states

involved in the transitions 26*p* → 26*s*, 32*p* → 32*s*, and 40*p* → 40*s*, and the applied fields

employed for the respective *p*-state excitations, we obtain the maximum possible transition

energy variations due to the inhomogeneous electric field. These are 4.9, 13, and 30 MHz

for the 26$p$, 32$p$, and 40$p$ initial states, respectively. Accordingly, for the $p$-state decays, the maximum energy variations due to the field are comparable to, but up to a factor of 1.7× larger than, those due to dipole-dipole interactions. Given our likely overestimate of the field inhomogeneity, both may play a role in suppressing collective emission from the ensemble.

## 4.4 Conclusion

We have studied the decay of Rydberg excitations in a cold Rb gas and find no evidence for the dramatic decrease in lifetimes predicted by Wang et al. [39]. The decay rates and population redistribution we observe are consistent with a model that considers only spontaneous emission from, and blackbody redistribution within, isolated atoms. In our experiments, a small electric field in the interaction region ejects any free electrons or ions from the excitation volume, preventing ionization or population transfer due to interactions with charged particles. In addition, the lack of spatial overlap between the trapping lasers and the Rydberg excitation laser well outside of the cold atom cloud ensures that there is no Rydberg excitation within an extended volume of lower-density, background Rb atoms in the chamber. Suppression of superradiant emission is likely due to variations in transition energies across the cold Rydberg atom sample. For initial $s$ states, these variations are dominated by inhomogeneities in DD exchange interactions within the random ensemble. Such inhomogeneities will necessarily be present in any measurement involving a large number of atoms where the separation between atoms is not well defined. For initial $p$ states, the suppression is likely due to a combination of DD exchange and electric field inhomogeneities.

# Bibliography

[1]   T. F. Gallagher, Rydberg Atoms, 1st ed. (Cambridge University Press, Cambridge, 1994).

[2]   M. D. Lukin, M. Fleischhauer, R. Cote, L. M. Duan, D. Jaksch, J. I. Cirac, and P. Zoller, Phys. Rev. Lett. 87, 037901 (2001).

[3]   D. Tong, S. M. Farooqi, J. Stanojevic, S. Krishnan, Y. P. Zhang, R. Cote, E. E. Eyler, and P. L. Gould, Phys. Rev. Lett. 93, 063001 (2004).

[4]   F. Robicheaux and J. V. Hernandez, Phys. Rev. A 72, 063403 (2005).

[5]   T. Cubel Liebisch, A. Reinhard, P. R. Berman, and G. Raithel, Phys. Rev. Lett. 95, 253002 (2005).

[6]   T. Vogt, M. Viteau, J. Zhao, A. Chotia, D. Comparat, and P. Pillet, Phys. Rev. Lett. 97, 083003 (2006).

[7]   E. Urban, T. A. Johnson, T. Henage, L. Isenhower, D. D. Yavuz, T. G. Walker, and M. Saffman, Nat. Phys. 5, 110 (2009).

[8]   Alpha Gaëtan, Yevhen Miroshnychenko, Tatjana Wilk, Amodsen Chotia, Matthieu Viteau, Daniel Comparat, Pierre Pillet, Antoine Browaeys, and Philippe Grangier, Nat. Phys. 5, 115 (2009).

[9]   T. Wilk, A. Gaetan, C. Evellin, J. Wolters, Y. Miroshnychenko, P. Grangier, and A. Browaeys, Phys. Rev. Lett. 104, 010502 (2010).

[10]  Hendrik Weimer, Robert Low, Tilman Pfau, and Hans Peter Buchler, Phys. Rev. Lett. 101, 250601 (2008).

[11]  M. Saffman and K. Molmer, Phys. Rev. Lett. 102, 240502 (2009).

[12] Robert Low, Hendrik Weimer, Ulrich Krohn, Rolf Heidemann, Vera Bendkowsky, Bjorn Butscher, Hans Peter Buchler, and Tilman Pfau, Phys. Rev. A 80, 033422 (2009).

[13] T. Pohl and P. R. Berman, Phys. Rev. Lett. 102, 013004 (2009).

[14] Thomas Amthor, Christian Giese, Christoph S. Hofmann, and Matthias Weidemuller, Phys. Rev. Lett. 104, 013001 (2010).

[15] T. Pohl, E. Demler, and M. D. Lukin, Phys. Rev. Lett. 104, 043002 (2010).

[16] S. Wuster, C. Ates, A. Eisfeld, and J. M. Rost, Phys. Rev. Lett. 105, 053004 (2010).

[17] Jens Honer, Hendrik Weimer, Tilman Pfau, and Hans Peter Buchler, Phys. Rev. Lett. 105, 160404 (2010).

[18] J. D. Pritchard, D. Maxwell, A. Gauguet, K. J. Weatherill, M. P. A. Jones, and C. S. Adams, Phys. Rev. Lett. 105, 193603 (2010).

[19] A. Schwarzkopf, R. E. Sapiro, and G. Raithel, Phys. Rev. Lett. 107, 103001 (2011).

[20] S. Sevincli, N. Henkel, C. Ates, and T. Pohl, Phys. Rev. Lett. 107, 153001 (2011).

[21] F. Bariani, Y. O. Dudin, T. A. B. Kennedy, and A. Kuzmich, Phys. Rev. Lett. 108, 030501 (2012).

[22] Matthieu Viteau, Paul Huillery, Mark G. Bason, Nicola Malossi, Donatella Ciampini, Oliver Morsch, Ennio Arimondo, Daniel Comparat, and Pierre Pillet, Phys. Rev. Lett. 109, 053002 (2012).

[23] D. D. Bhaktavatsala Rao and Klaus Molmer, Phys. Rev. Lett. 111, 033606 (2013).

[24] H. Schempp, G. Gunter, M. Robert-de-Saint-Vincent, C. S. Hofmann, D. Breyel, A. Komnik, D. W. Schonleber, M. Garttner, J. Evers, S. Whitlock, and M. Weidemuller, Phys. Rev. Lett. 112, 013002 (2014).

[25] Matthew Ebert, Alexander Gill, Michael Gibbons, Xianli Zhang, Mark Saffman, and Thad G. Walker, Phys. Rev. Lett. 112, 043602 (2014).

[26] D. Paredes-Barato and C. S. Adams, Phys. Rev. Lett. 112, 040501 (2014).

[27] H. Gorniaczyk, C. Tresp, J. Schmidt, H. Fedder, and S. Hofferberth, Phys. Rev. Lett. 113, 053601 (2014).

[28] Daniel Tiarks, Simon Baur, Katharina Schneider, Stephan Dürr, and Gerhard Rempe, Phys. Rev. Lett. 113, 053602 (2014).

[29] David Petrosyan and Klaus Molmer, Phys. Rev. Lett. 113, 123003 (2014).

[30] J. Pellegrino, R. Bourgain, S. Jennewein, Y. R. P. Sortais, A. Browaeys, S. D. Jenkins, and J. Ruostekoski, Phys. Rev. Lett. 113, 133602 (2014).

[31] Daniel Barredo, Henning Labuhn, Sylvain Ravets, Thierry Lahaye, Antoine Browaeys, and Charles S. Adams, Phys. Rev. Lett. 114, 113002 (2015).

[32] Y. O. Dudin and A. Kuzmich, Science 336, 887 (2012).

[33] Alexander W. Glaetzle, Marcello Dalmonte, Rejish Nath, Christian Gross, Immanuel Bloch, and Peter Zoller, Phys. Rev. Lett. 114, 173002 (2015).

[34] R. M. W. van Bijnen and T. Pohl, Phys. Rev. Lett. 114, 243002 (2015).

[35] M. Ebert, M. Kwon, T. G. Walker, and M. Saffman, Phys. Rev. Lett. 115, 093601 (2015).

[36] F. Gounand, M. Hugon, P. R. Fournier, and J. Berlande, J. Phys. B 12, 547 (1979).

[37] C. Carr, R. Ritter, C. G. Wade, C. S. Adams, and K. J. Weatherill, Phys. Rev. Lett. 111, 113901 (2013).

[38] R. H. Dicke, Phys. Rev. 93, 99 (1954).

[39] T. Wang, S. F. Yelin, R. Cote, E. E. Eyler, S. M. Farooqi, P. L. Gould, M. Kostrun, D. Tong, and D. Vrinceanu, Phys. Rev. A 75, 033802 (2007).

[40] N. Skribanowitz, I. P. Herman, J. C. MacGillivray, and M. S. Feld, Phys. Rev. Lett. 30, 309 (1973).

[41] M. Gross, C. Fabre, P. Pillet, and S. Haroche, Phys. Rev. Lett. 36, 1035 (1976).

[42] D. Pavolini, A. Crubellier, P. Pillet, L. Cabaret, and S. Liberman, Phys. Rev. Lett. 54, 1917 (1985).

[43]  M. G. Moore and P. Meystre, Phys. Rev. Lett. 83, 5202 (1999).

[44]  J. I. Kim, R. B. B. Santos, and P. Nussenzveig, Phys. Rev. Lett. 86, 1474 (2001).

[45]  C. Greiner, B. Boggs, and T. W. Mossberg, Phys. Rev. Lett. 85, 3793 (2000).

[46]  Chiu Fan Lee and Neil F. Johnson, Phys. Rev. Lett. 93, 083001 (2004).

[47]  Vasily V. Temnov and Ulrike Woggon, Phys. Rev. Lett. 95, 243602 (2005).

[48]  J. O. Day, E. Brekke, and T. G. Walker, Phys. Rev. A 77, 052712 (2008).

[49]  Kirill Prozument, Anthony P. Colombo, Yan Zhou, G. B. Park, Vladimir S. Petrovic, Stephen L. Coy, and Robert W. Field,   Phys. Rev. Lett. 107, 143001 (2011).

[50]  Anthony P. Colombo, Yan Zhou, Kirill Prozument, Stephen L. Coy, and Robert W. Field, J. Chem. Phys. 138, 014301 (2013).

[51]  Florian Karlewski, Markus Mack, Jens Grimmel, Nora Sandor, and Jozsef Fortagh, Phys. Rev. A 91, 043422 (2015).

[52]  N. E. Rehler and J. H. Eberly, Phys. Rev. A 3, 1735 (1971).

[53]  R. Bonifacio and L. A. Lugiato, Phys. Rev. A 11, 1507 (1975).

[54]  Zhi-Gang Feng, Lin-Jie Zhang, Jian-Ming Zhao, Chang-Yong Li, and Suo-Tang Jia, J. Phys. B 42, 145303 (2009).

[55]  K. J. Weatherill, J. D. Pritchard, R. P. Abel, M. G. Bason, A. K. Mohapatra, and C. S. Adams, J. Phys. B 41, 201002 (2008).

[56]  Jianing Han and H. Maeda, Can. J. Phys. 92, 1130 (2014).

[57]  M. R. Kutteruf, Coherence in Rydberg atoms: Measurement and Control, Ph.D. dissertation, University of Virginia (2010).

[58]  B. G. Richards and R. R. Jones (unpublished).

[59]  Wenhui Li, Michael W. Noel, Michael P. Robinson, Paul J.   Tanner, Thomas F. Gallagher, Daniel Comparat, Bruno Laburthe Tolra, Nicolas Vanhaecke, Thibault Vogt, Nassim Zahzam, Pierre Pillet, and Duncan A. Tate, Phys. Rev. A 70, 042713 (2004).

[60] M. P. Robinson, Interactions in a frozen Rydberg gas, Ph.D. dissertation, University of Virginia, 2002.

[61] F. Gounand, J. Phys. (Paris) 40, 457 (1979).

[62] M. Gross and S. Haroche, Phys. Rep. 93, 301 (1982).

[63] M. R. Kutteruf and R. R. Jones, Phys. Rev. A 82, 063409 (2010).

[64] M. R. Kutteruf and R. R. Jones, Phys. Rev. Lett. 108, 013001 (2012).

[65] M. L. Zimmerman, M. G. Littman, M. M. Kash, and D. Kleppner, Phys. Rev. A 20, 2251 (1979).

# 5 Rydberg Wavepackets Evolution in A Frozen Gas of DD Coupled Atoms

We have studied the evolution of Rydberg wavepackets in the presence of interatomic dipole- dipole interactions in a frozen Rb gas. Rb atoms in a MOT are first laser-excited to *ns* Rydberg eigenstates. A picosecond THz pulse further excites them into coherent superposition states involving the initial-level and neighboring np-states. A second, identical, time-delayed THz pulse probes the wavepacket dynamics. As the wavepackets evolve they are influenced by dipole-dipole interactions, predominantly pairwise excitation-exchange processes of the form $|s\rangle|p\rangle \leftrightarrow |p\rangle|s\rangle$. The coherent electronic evolution of the ensemble dephases due to the variation in dipole-dipole coupling strength between atom pairs in the MOT. The experimental results are in good agreement with numerical calculations that simulate the interactions between nearest neighbors in a frozen gas.

# 5.1 Introduction

As we mentioned in Chapter 3, the large size of Rydberg atoms endows them with extreme properties which, when properly harnessed, can be exploited to study fundamental problems and applications involving the quantum control of matter in single-, few-, and many-body systems. For example, Rydberg atoms are highly-sensitivity to applied electric fields and, accordingly, to neighboring atoms, as these can induce substantial energy-shifts and/or quantum-state modification. They also exhibit long electronic time-scales, $\tau = 2\pi/E$, which characterize the evolution of superpositions of Rydberg states with small energy separations, $E$.

The strong, long-range dipole-dipole interactions that exist between neighboring Rydberg atoms couple their electronic and center-of-mass degrees of freedom [1]. Control over this coupling could enable coherent manipulation of multi-atom correlations and entanglement [2–13] with potential applications to quantum information processing [14–18] or explorations of few- and many-body quantum mechanics. That said, the time- and energy-scales associated with electronic motion within individual atoms can differ substantially from those relevant to dipole-dipole couplings between atoms [1]. This disparity of scales has encouraged the segregation of work in this area, with studies of electron dynamics within atoms performed separately from those investigating interactions between atoms.

For example, in experiments exploring interactions between Rydberg atoms (e.g. resonant energy transfer [19–30], dipole blockade [2, 13, 31–36], quantum-logic gate implementation [14–18]) the interatomic coupling strengths typically range from kHz to tens of MHz with associated time-scales for the development of correlations ranging from tens of nanoseconds to milliseconds. Frequency-domain techniques and cold atomic ensembles are usually employed to enable selective excitation or high-resolution

spectroscopy of the few- or many-body eigenstates and to limit effects associated with atom motion. Since the coupling between atoms depends on their separation, both Rydberg atom density, $\rho$ and temperature, $T$, play an important role as these determine the strength and length-scales of correlations as well as the time-scales over which coherence can be maintained.

Conversely, experiments aimed at coherently manipulating and viewing the evolution of one-electron [37–41] and two-electron [42–52] Rydberg wavepackets typically utilize time- domain methods involving ultra-fast optical and/or electric-field pulses to first excite coherent superposition states and then probe their behavior. For atoms with principal quantum number $n$ <100 or so, the relevant dynamics in these experiments usually fall in the picosecond or femtosecond regime. Over these time-scales relative atom motion is completely negligible, even in thermal beams. Moreover, interactions between atoms can be ignored since their influence on the electronic evolution develops only after orders of magnitude longer times (tens of nanoseconds to milliseconds).

More generally, however, both ultrafast electron evolution and atom-atom correlations play a role in the quantum dynamics of Rydberg systems. Electron dynamics in isolated atoms set the scale for how rapidly correlations between atoms can be modified, whereas the coupling between atoms determines the minimum-time required for entanglement between pairs or groups of atoms to influence electronic evolution within them. Accordingly, potential applications may require the coherent manipulation of groups, pairs, or individual Rydberg atoms over time- and energy- scales spanning many orders of magnitude. Thus, these systems provide challenging platforms on which to explore few- and many-body quantum control.

As a step towards addressing this problem, we examine the influence of strong, resonant dipole-dipole interactions between atoms on the evolution of Rydberg wavepackets within

those atoms. Specifically, we consider the pulsed, coherent excitation of atoms from a Rydberg eigenstate $|s\rangle$, to an adjacent level of opposite parity, $|p\rangle$, at at time $t = 0$. In an extremely diffuse ensemble where the separation between atoms $R \rightarrow \infty$, the excitation would result in the creation of identical Rydberg wavepackets in each atom

$$\Psi(t) = cos\theta|s\rangle + e^{-i(Et+\phi)}sin\theta|p\rangle \tag{5.1}$$

where $E$ is the energy separation between the eigenstates, $\theta$ is an admixture coefficient, $\phi$ is an arbitrary phase related to the details of the excitation and, unless otherwise noted, atomic units are used throughout. The wavepackets are characterized by identical time-dependent electric dipole-moments which oscillate with a period, $\tau = 2\pi/E$.

At higher densities the Rydberg electrons on each atom do not evolve independently. Each electron is affected by the multi-pole fields produced by neighboring Rydberg atoms [1]. The correlations resulting from these interactions can be non-negligible even for separations $R$ of several microns or more [30]. In the density regime explored here, $10^8 \times$ cm$^{-3} < \rho < 3 \times 10^9$ cm$^{-3}$, $R \gg r_0$ where $r_0 \sim 2n^2$ is the radial extent of the Rydberg wavefunction on each atom. Accordingly, resonant dipole-dipole exchange between nearest-neighbor atoms [23, 24, 27, 53] with a coupling strength on the order of $n^4/R^3$ ( $\sim$5 MHz at $n$=30 and $\rho = 10^9$ $cm^{-3}$), dominates the atom-atom interaction. The coupling alters the eigenstates of atom pairs and, accordingly, modifies the electric-dipole oscillations within them. We measure, as a function of density, the influence of the dipole-dipole exchange interaction on the coherent dipole oscillations in the Rydberg ensemble.

## 5.2 Experimental Procedure

In Chapter 2, we talked about the general experiment setup. More details about the experimental approach of this project is provide below.

In the experiments, $^{85}Rb$ atoms at ~ 70 $\mu$K in a magneto-optical trap (MOT) are laser-excited from the $5p_{3/2}$ upper cycling-level to the $32s$ Rydberg state. The atoms are then exposed to a picosecond THz pulse which coherently redistributes a fraction ~ 20% of the $32s$ population to neighboring $31p$ and $32p$ levels which lie approximately $4.79 cm^{-1}$ and $4.35 cm^{-1}$ below and above the initial state, respectively. Excitation of other levels is negligible. The mixed-parity Rydberg wavepackets are allowed to freely evolve for a variable time $\Delta t$ before they are subjected to a second, identical THz pulse. The probability amplitude transfer during the second THz pulse interferes with that from the first, resulting in a $\Delta$t-dependent modulation in the net population in each Rydberg state. State-selective field ionization (SSFI) is used to measure the final Rydberg eigenstate distribution as a function of $\Delta t$ and $\rho$.

The initial Rydberg excitation is performed using a 10 ns, dye-amplified pulse from a ~ 482 nm cw diode laser. A 10ns pulse is sliced from the cw laser by applying a high-voltage pulse to a Pockells cell that is positioned between crossed polarizers. The two-stage dye-amplifier is pumped at 15 Hz by the third harmonic of a Nd:YAG laser. The 482nm laser pulse is focused into the MOT using a 500 mm spherical lens. The freely propagating picosecond THz pulses are produced via optical rectification of 2 mJ, 150 fs, 790 nm laser pulses in $LiNbO_3$, using a tilted-pulse-front pumping scheme [54, 55]. The 790nm pulses are generated in a 15 Hz Ti:Sapphire regenerative amplifier. A Michelson interferometer, with a variable-length delay-stage in one arm, is used to split each 790 nm pulse into a pump- probe pair with a delay $0 \leqslant \Delta t < 16$ ns. The two 790 nm pulses are collinearly incident on the $LiNbO_3$ crystal, producing a pair of identical, co-propagating broadband single-cycle THz pulses [56]. After exiting the $LiNbO_3$ crystal, the THz beam is collected by a 50 mm diameter, 50 mm focal length off-axis paraboloid. It is then weakly focused by a Teflon lens, through a thin fused silica window, into the MOT. The ramped-field that

performs the SSFI is applied to the atoms approximately 100 ns after the second THz pulse. Four thin, parallel, stainless steel rods are positioned in a rectangular array surrounding the 0.5 mm diameter atom cloud, and enable the application of a spatially-uniform field while providing optical access for the trapping beams, Rydberg excitation laser, and THz pulses. Rb ions produced during the field ramp are pushed toward a micro-channel plate detector and, in principle, population in different Rydberg states can be distinguished by different ionization times in the ramped field. In practice, the signals associated with the 32$s$ and 31$p$ states appear at the same time, thus we do not separately measure the populations in these two states. The delay, $\Delta t$ between the THz pulses is scanned continuously while integrating the SSFI signals across two time bins, yielding the populations in 32$s$+31$p$ states and 32$p$ level, respectively. The Rydberg atom density, $10^8$ cm$^{-3}$< $\rho$ < $3 \times 10^9$ cm$^{-3}$, is varied by changing the current to the getters that supply the Rb atoms to the MOT. At these densities, with $T = 70$ $\mu$K, relative atom motion due to thermal energy or dipole-dipole forces is negligible during the ~ 100 ns duration of the experiments.

## 5.3 Experimental Results

Figure 5.1 shows the measured population in the 32$s$+31$p$ states as a function of the delay $\Delta t$ between the two THz pulses. The modulations in the population have a frequency of 4.35 cm$^{-1}$, corresponding to the energy separation between the 32$s$ and the 32$p$ states, and reflect the oscillation of the electric dipole-moment of the wavepacket that is created by the first THz pulse. Oscillations at the same frequency are observed in the 32$p$ population, but are 180 degrees out of phase. The modulations can be interpreted as the result of time-domain Ramsey interference in the 32$s$ and 32$p$ amplitudes created by the first and second THz pulses [57, 58]. Accordingly, the amplitude of the oscillations provides a measure of the macroscopic wavepacket coherence. Although the broadband THz pulses also excites atoms from 32$s$ to 31$p$ we do not observe any significant signal

modulations at 4.79 cm$^{-1}$, the frequency corresponding to the $32s - 31p$ energy interval. For the weak population transfers studied here, any oscillations in the $32s$ population would be out of phase with those in $31p$, resulting in no net modulation in the combined $32s+31p$ signal that we detect. Moreover, the small variations in the $32s$ amplitude associated with the $31p$ excitation have negligible influence on the population transfer to $32p$, so no 4.79 cm$^{-1}$ beat is observed in the $32p$ signal.
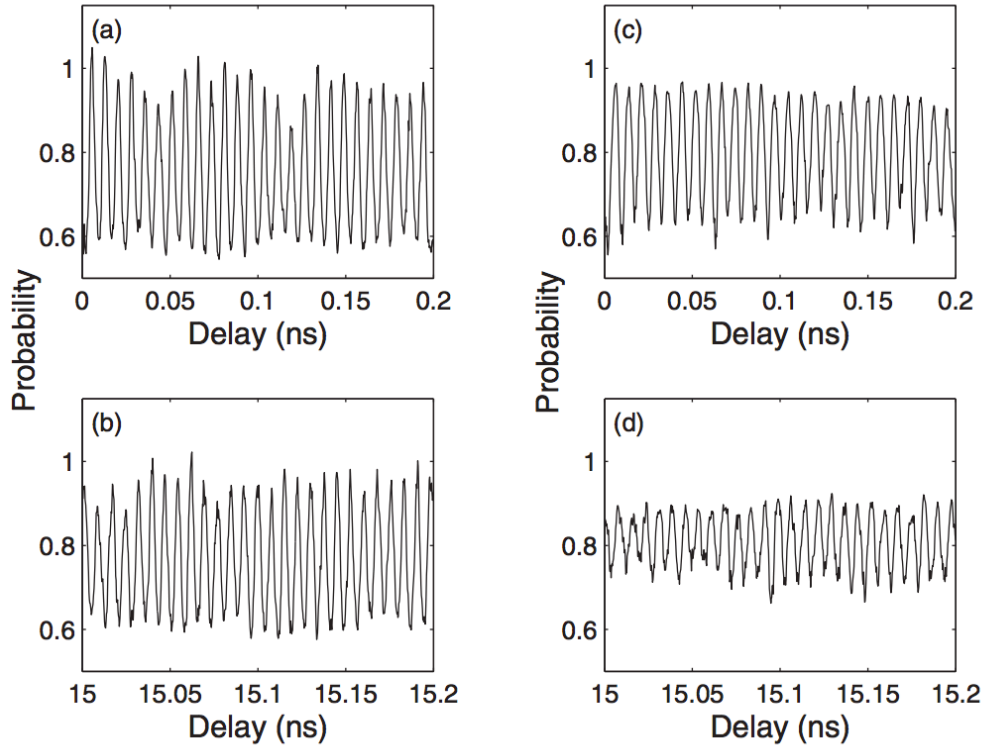


Figure 5.1: Measured population in the combined $32s+31p$ states as a function of the delay $\Delta t$ between two THz pulses. The left panels show data collected at low Rydberg density, $\rho \sim 3 \times 10^8$ cm$^{-3}$, for (a) short ($\Delta t \simeq 0$) and (b) long ($\Delta t \simeq 15$ns) delays, respectively. The right panels show data collected at high Rydberg density, $\rho \sim 2 \times 10^9$ cm$^{-3}$, for c) short ($\Delta t \simeq 0$) and d) long ($\Delta t \simeq 15$ns) delays, respectively. The decrease in oscillation amplitude at high density and long delays is apparent.

Figure 5.1a and 5.1b show the situation at low density $\rho \sim 3 \times 10^8$ cm$^{-3}$ for short ($\Delta t \simeq$ 0) and long ($\Delta t \simeq$ 15 ns) delays, respectively. Analogous plots at higher density $\rho \sim 2 \times 10^9$ cm$^{-3}$ are shown in Figure 5.1c and 5.1d. At low density, the average oscillation amplitudes are similar at short and long delays. However, at higher densities, there is a notable decrease in oscillation amplitude with increasing delay. This density-dependent decay in the macroscopic wavepacket coherence, i.e. dephasing, is the principal focus of this paper.

To quantify the average oscillation amplitude during a given time interval, we Fourier transform the delay-dependent data, and compute the area under the spectral feature (between 4.0 cm$^{-1}$ and 4.6 cm$^{-1}$) corresponding to the $32s - 32p$ quantum beat. Figure 5.2 shows the Fourier transforms of the data in Figure 5.1. For each Rydberg density, we compute a decay factor, $\eta$, defined as the ratio of the spectral area measured near $\Delta t = $ 15ns to that measured near $\Delta t = 0$.
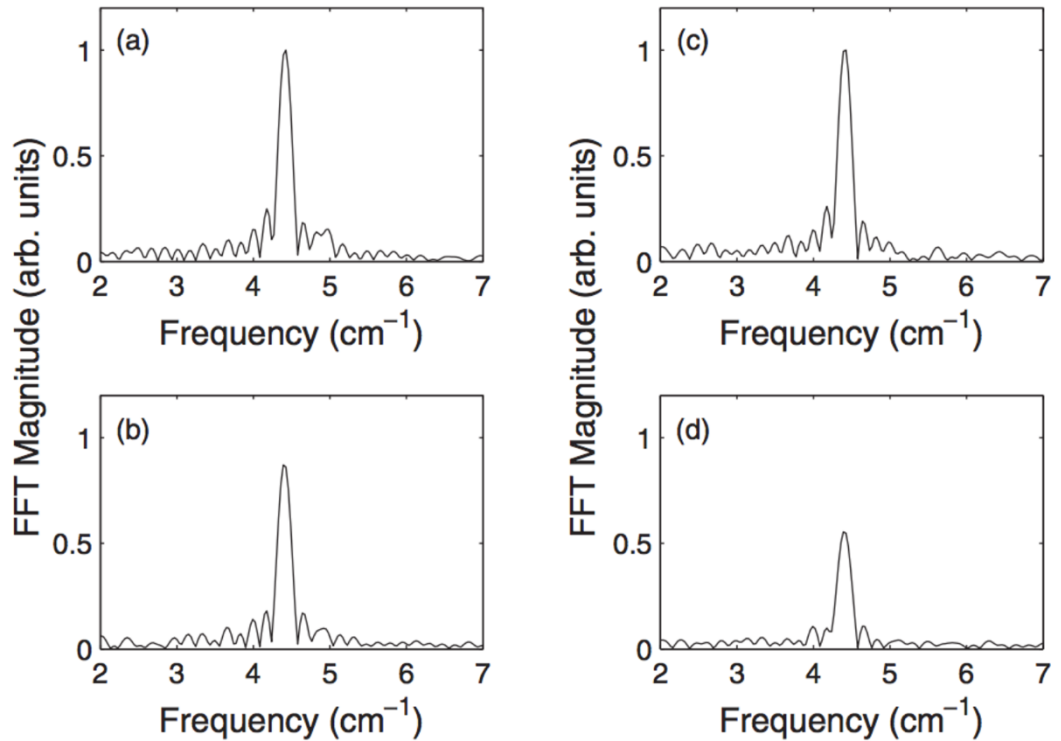


Figure 5.2: Fast Fourier transform (FFT) of the delay-dependent populations shown in Figure 5.1.

The experimentally determined values of $\eta$ are plotted vs Rydberg density in Figure 5.3 along with the results of a quantum simulation that considers the dipole-dipole interaction between nearest neighbor atoms in a frozen ensemble of randomly distributed Rydberg atoms. The simulation is in good agreement with the measurements. Before discussing the details of the full simulation, we present a simple model that captures the essential physics. Namely, the decrease in $\eta$ with increasing density is due to the variation in the strength of the dipole-dipole exchange interaction for different pairs of nearest neighbor atoms.
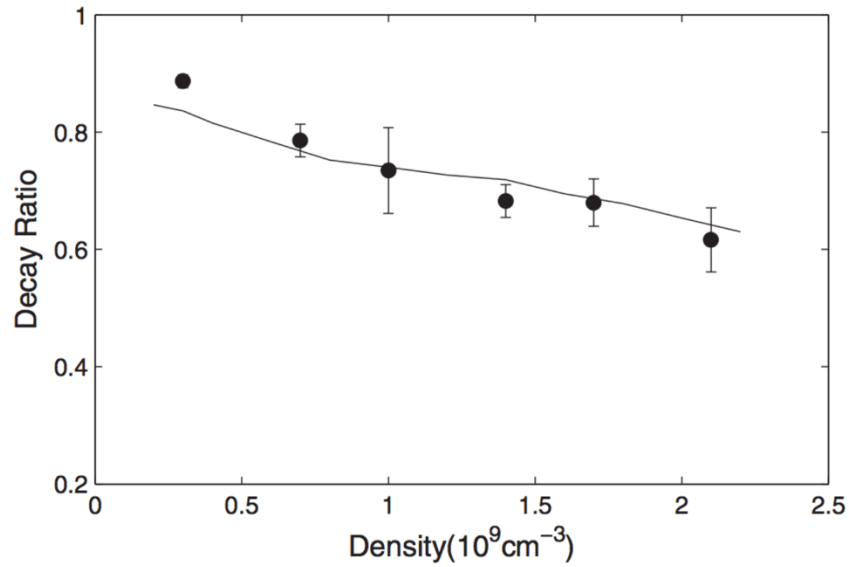


Figure 5.3: Measured (filled circles) and simulated (solid curve) decay ratio, $\eta$, as a function of Rydberg density.

## 5.4 Discussion

Consider a two-level Rydberg atom with opposite parity, non-degenerate eigenstates, $|s\rangle$ and $|p\rangle$, that are split by an energy $E_0$. Ignoring the azimuthal degrees of freedom, the eigenstates for a pair of atoms with a large separation $R \rightarrow \infty$ are: $|ss\rangle$, $|sp\rangle$, $|ps\rangle$, and $|pp\rangle$, with energies as shown on the left in Figure 5.4. For smaller values of $R$, the pair eigenstates

are modified due to the interactions between the atoms. Provided that $R$ remains sufficiently large that the Rydberg wavefunctions of the individual atoms do not overlap, the predominant interaction between the atoms is given by the dipole-dipole coupling [53],

$$V = [\vec{\mu_A} \cdot \vec{\mu_B} - 3(\vec{\mu_A} \cdot \hat{R})(\vec{\mu_B} \cdot \hat{R})]/R^3 \qquad (5.2)$$

as we mentioned in Chapter 4. The matrix elements coupling $|ss\rangle$ or $|pp\rangle$ to $|sp\rangle$ and $|ps\rangle$ are identically zero. In addition, provided $2E_0$ is much greater than the magnitude of the matrix element connecting $|ss\rangle$ and $|pp\rangle$, the Hamiltonian is approximately diagonalized by considering only the coupling between the degenerate states $|sp\rangle$, $|ps\rangle$, i.e. the dipole-dipole exchange interaction. The modified energy levels are shown on the right in Figure 5.4, with eigenstates $|+\rangle$ and $|-\rangle$ corresponding to symmetric and antisymmetric combinations of $|sp\rangle$, $|ps\rangle$. The exchange splitting between this pair of entangled states is $2\epsilon = 2\langle ps|V|sp\rangle$ which implicitly depends on the atom separation, $R$.

A THz pulse with a central frequency $E_0$ and a bandwidth $\gg \epsilon$ can excite the atom pair from $|ss\rangle$ to $|+\rangle$, via a one-photon excitation, or to $|pp\rangle$ through two-photon absorption. However, $|-\rangle$ is not populated since the transition matrix elements connecting it to all other levels are identically zero. For a relatively weak THz pulse, the $|pp\rangle$ excitation probability is negligible, so an electronic coherence is established between $|ss\rangle$ and $|+\rangle$, and the electronic wavefunction has the form, $\Psi(t) = cos\theta|ss\rangle + e^{-i(Et+\phi)}sin\theta|+\rangle$, where $\theta$ depends on the excitation probability and $\phi$ is an excitation phase. This wavepacket has the same form as the single electron wavepacket in Equation (5.1) and, similarly, is characterized by a time-dependent dipole moment which oscillates sinusoidally at a frequency, $E = E_0 + \epsilon$. When the atoms are exposed to a second THz pulse, the net population transfer from $|ss\rangle$ to $|+\rangle$ is delay- dependent, oscillating at a frequency $E$. This modulation can be observed in the total population of individual atoms in states $|s\rangle$ or $|p\rangle$. It can be viewed as the result of time- domain Ramsey interference in the probability

amplitude transferred from $|ss\rangle$ to $|+\rangle$ in each of the two THz pulses [57, 58]. Alternatively, but equivalently, it can be attributed to the variations in the wavepacket's instantaneous electric dipole moment during the second THz pulse.
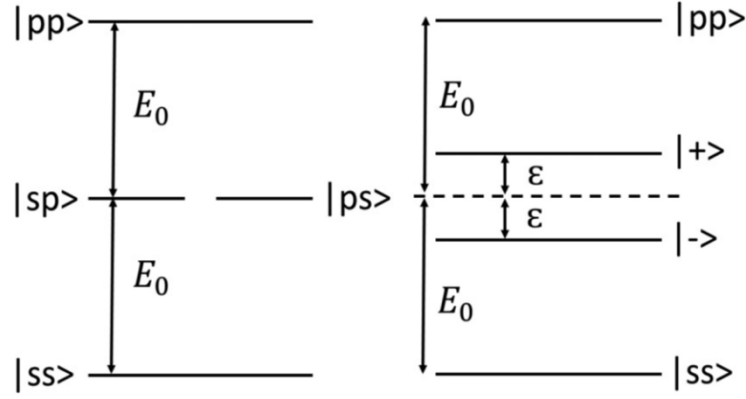


Figure 5.4: Schematic energy level diagram for the eigenstates of a pair of two level atoms. The diagrams on the left and right sides of the figure depict the situation at large and small interatomic spacing, *R*, respectively.

In a random ensemble of atoms, the dominant coupling is between each atom and its nearest neighbor. Due to the variation in *R* for different atom pairs, there is a broad distribution of dipole-dipole exchange energies $2\epsilon$ and, accordingly, a range of wavepacket oscillation frequencies E across the sample. This inhomogeneity results in a dephasing of the detected oscillations in the $|s\rangle$ and $|p\rangle$ populations. The dephasing time decreases with increasing Rydberg density, since the range of possible exchange energies grows with the probability of finding atom pairs with smaller *R*. It is important to note, however, that the macroscopic dephasing is not an indicator of microscopic decoherence of individual atom pairs.

In the experiments, limitations in the maximum path length difference in the arms of the Michelson interferometer preclude our measurement of the wavepacket evolution from

its initiation through complete dephasing. Instead, we use $\eta$ as a measure of the dephasing rate. Since smaller values of $\eta$ reflect more rapid dephasing, the data in Figure 5.3 confirm the qualitative prediction of the model presented in the preceding paragraphs.

To determine if nearest neighbor interactions are sufficient to cause the density-dependent dephasing that is observed, we perform quantum simulations to obtain a quantitative prediction of the dephasing rate. Specifically, we numerically integrate the time-dependent Schroedinger equation to calculate the delay-dependent probability for finding atoms in a range of essential Rydberg states following the exposure of a random ensemble of $32s$ atoms to two single-cycle THz pulses [56] like those used in the experiments. We include $33s$, $32p$, $32s$, and $31p$ states, with fine-structure, and consider the excitation to, and from, Rydberg-Rydberg pairs with all allowable values of $M$, the quantum number corresponding to the projection of total angular momentum along $\vec{R}$. Atom pairs with different $M$ possess different interaction energies, even for the same value of $R$, providing an additional source of inhomogeneity in the oscillation frequency of different wavepackets in the ensemble [29, 59]. Radial matrix elements are computed using a Numerov algorithm [60] with the known quantum defects of the Rb $ns$ and $np$ states. The simulation results for individual atom pairs are integrated over the nearest neighbor distribution function for $R$ for a given Rydberg density [61]. Since the quantization axis for each atom pair is chosen to lie along $\vec{R}$, the THz polarization angle relative to that axis is varies from one atom pair to the next (refer to 3.3.4). We find that the simulation results are insensitive to whether we explicitly perform the calculation over all polarization angles and average those results, or if we fix the polarization angle at a value for which the interaction potential is equal to angle-averaged value. Since the latter method substantially improves the calculation speed, we use it for the results shown in Figure 5.3.

Inspection of Figure 5.3 shows that the agreement between the data and simulation is good. The fact that there are no adjustable parameters in the calculation, indicates that

nearest neighbor interactions are sufficient to explain the observed dephasing. Beyond the limited pump-probe delay range available to the experiment, the simulations show that the degree and rate of dephasing continue to increase at longer delays and at higher densities, respectively.

## 5.5 Conclusion

We have explored the evolution of Rydberg wavepackets in the presence of strong dipole-dipole interactions in a frozen gas. The time-scales associated with oscillation of the Rydberg electric dipole moment (~ 8 ps) and the interatomic excitation exchange (~ 200 ns) differ by over four orders of magnitude yet we are able to probe the system for a sufficiently long time to observe the influence of the atom-atom coupling. The distribution of atom separations results in an inhomogeneity in the strength of the exchange coupling between neighboring atoms, causing a rapid dephasing of the macroscopic coherence. In analogy to recent work with cold polar molecules [62], future experiments may take advantage of optical confinement of atoms at well-defined separations to explore the use of the dipole-dipole coupling as a controllable tool for manipulating multi-electron correlation and dynamics.

# Bibliography

[1]     T. F. Gallagher, Rydberg Atoms, 1st ed. (Cambridge University Press, Cambridge, 1994).

[2]     M. D. Lukin, M. Fleischhauer, R. Cote, L.M. Duan, D. Jaksch, J.I. Cirac, and P. Zoller, Phys. Rev. Lett. 87, 037901 (2001).

[3]     T. Wilk, A. Gaetan, C. Evellin, J. Wolters, Y. Miroshnychenko, P. Grangier, and A. Browaeys, Phys. Rev. Lett. 104, 010502 (2010).

[4]     Hendrik Weimer, Robert Low, Tilman Pfau, and Hans Peter Buchler, Phys. Rev. Lett. 101, 250601 (2008).

[5]     T. Pohl, E. Demler, and M. D. Lukin, Phys. Rev. Lett. 104, 043002 (2010).

[6]     S. Wuster, C. Ates, A. Eisfeld, and J. M. Rost, Phys. Rev. Lett. 105, 053004 (2010).

[7]     Jens Honer, Hendrik Weimer, Tilman Pfau, and Hans Peter Buchler, Phys. Rev. Lett. 105, 160404 (2010).

[8]     A. Schwarzkopf, R. E. Sapiro, and G. Raithel, Phys. Rev. Lett. 107, 103001 (2011).

[9]     Matthieu Viteau, Paul Huillery, Mark G. Bason, Nicola Malossi, Donatella Ciampini, Oliver Morsch, Ennio Arimondo, Daniel Comparat, and Pierre Pillet, Phys. Rev. Lett. 109, 053002 (2012).

[10]    D.D.Bhaktavatsala Rao and K. Molmer, Phys. Rev. Lett. 111, 033606 (2013).

[11]    M. Ebert, A. Gill, M. Gibbons, X. Zhang, M. Saffman, and T.G. Walker, Phys. Rev. Lett. 112, 043602 (2014).

[12]    H. Schempp, G. Gunter, M. Robert-de-Saint-Vincent, C.S. Hofmann, D. Breyel, A. Komnik, D.W. Schonleber, M. Garttner, J. Evers, S. Whitlock, and M. Weidemuller, Phys. Rev. Lett. 112 013002 (2014).

[13]  D. Barredo, S. Ravets, H. Labuhn, L. Beguin, A. Vernier, F. Nogrette, T. Lahaye, and A. Browaeys, Phys. Rev. Lett. 112, 183002 (2014).

[14]  D. Jaksch, J.I. Cirac, P. Zoller, S.L. Rolston, R. Cote, and M.D. Lukin, Phys. Rev. Lett. 85, 2208 (2000).

[15]  M. Muller, I. Lesanovsky, H. Weimer, H. P. Buchler, and P. Zoller, Phys. Rev. Lett. 102, 170502 (2009).

[16]  M. Saffman, T.G. Walker, and K. Molmer, Rev. Mod. Phys. 82, 2313 (2010), and references therein.

[17]  L. Isenhower, E. Urban, X. L. Zhang, A. T. Gill, T. Henage, T. A. Johnson, T. G. Walker, and M. Saffman, Phys. Rev. Lett. 104, 010503 (2010).

[18]  D. Paredes-Barato and C.S. Adams, Phys. Rev. Lett. 112, 040501 (2014).

[19]  K.A. Safinya, J. F. Delpech, F. Gounand, W. Sandner, and T.F. Gallagher, Phys. Rev. Lett. 47, 405 (1981).

[20]  P. Pillet, R. Kachru, N. H. Tran, W. W. Smith, and T. F. Gallagher, Phys. Rev. Lett. 50, 1763 (1983).

[21]  D.S. Thomson, M.J. Renn, and T.F. Gallagher, Phys. Rev. Lett. 65, 3273 (1990).

[22]  M.J. Renn and T.F. Gallagher, Phys. Rev. Lett. 67, 2287 (1991).

[23]  W.R. Anderson, J.R. Veale, and T.F. Gallagher, Phys. Rev. Lett. 80, 249 (1998).

[24]  I. Mourachko, D. Comparat, F. de Tomasi, A. Fioretti, P. Nosbaum, V. M. Akulin, and P. Pillet, Phys. Rev. Lett. 80, 253 (1998).

[25]  T. J. Carroll, K. Claringbould, A. Goodsell, M. J. Lim, and M. W. Noel, Phys. Rev. Lett. 93, 153001 (2004).

[26]  A. Walz-Flannigan, J. R. Guest, J.-H. Choi, and G. Raithel, Phys. Rev. A 69, 063405(2004).

[27]   S. Westermann, T. Amthor, A.L. de Oliveira, J. Deiglmayr , M. Reetz-Lamour, and M. Weidemuller, Eur. Phys. J. D 40, 37 (2006).

[28]  P. Bohlouli-Zanjani, J. A. Petrus, and J. D. D. Martin, Phys. Rev. Lett. 98, 203005 (2007).

[29]  M.R. Kutteruf and R.R. Jones, Phys. Rev. A 82, 063409 (2010).

[30]  M.R. Kutteruf and R.R. Jones, Phys. Rev. Lett. 108, 013001 (2012).

[31]  D. Tong, S.M. Farooqi, J. Stanojevic, S. Krishnan, Y.P. Zhang, R. Cote, E.E. Eyler, and P.L. Gould, Phys. Rev. Lett. 93, 063001 (2004).

[32]  K. Singer, M. Reetz-Lamour, T. Amthor, L.G. Marcassa, and M. Weidemuller, Phys. Rev. Lett. 93, 163001 (2004).

[33]  T. Cubel Liebisch, A. Reinhard, P. R. Berman, and G. Raithel, Phys. Rev. Lett. 95, 253002 (2005).

[34]  T. Vogt, M. Viteau, J. Zhao, A. Chotia, D. Comparat, and P. Pillet, Phys. Rev. Lett. 97, 083003 (2006).

[35]  E. Urban, T.A. Johnson, T. Henage, L. Isenhower, D.D. Yavuz, T.G. Walker and M. Saffman, Nature Physics 5, 110 (2009).

[36]  A. Gatan, Y. Miroshnychenko, T. Wilk, A. Chotia, M. Viteau, D. Comparat, P. Pillet, A. Browaeys and P. Grangier, Nature Physics 5, 115 (2009).

[37]  R.R. Jones and L.D. Noordam, Electronic Wavepackets, Adv. in At. Mol. Opt. Phys. 38, 1 (1997), and references therein.

[38]  F.B. Dunning, J.J. Mestayer, C.O. Reinhold, S. Yoshida, and J. Burgdorfer, J. Phy. B: At. Mol. Opt. Phys. 42, 022001 (2009), and references therein.

[39]  J. Bromage and C.R. Stroud, Jr., Phys. Rev. Lett. 83, 4963 (1999).

[40]  H. Maeda, D.V.L. Norum, and T.F. Gallagher, Science 307, 1757 (2005).

[41]  R.S. Minns, M.R. Kutteruf, H. Zaidi, L. Ko and R.R. Jones, Phys. Rev. Lett. 97, 040504 (2006).

[42]  J.G. Story, D.I. Duncan, and T.F. Gallagher, Phys. Rev. Lett. 71, 3431 (1993).

[43]  D. W. Schumacher, B. J. Lyons, and T. F. Gallagher, Phys. Rev. Lett. 78, 4359 (1997).

[44] Xin Chen and John A. Yeazell, Phys. Rev. Lett. 81, 5772 (1998).

[45] R. van Leeuwen, M.L. Bajema, and R.R. Jones, Phys. Rev. Lett. 82, 2852 (1999).

[46] J.B.M. Warntjes, C. Wesdorp, F. Robicheaux, and L.D. Noordam, Phys. Rev. Lett. 83, 512 (1999).

[47] J.E. Thoma and R.R. Jones, Phys. Rev. Lett. 83, 516 (1999).

[48] J.G. Story and H.N. Ereifej, Phys. Rev. Lett. 86, 612 (2001).

[49] R. van Leeuwen, K. Vijayalakshmi, and R.R. Jones, Phys. Rev. A 63, 033403 (2001).

[50] S.N. Pisharody and R.R. Jones, Phys. Rev. Lett. 91, 203002 (2003).

[51] S.N. Pisharody and R.R. Jones, Science 303, 813 (2004).

[52] X. Zhang, R.R. Jones, and F. Robicheaux, Phys. Rev. Lett. 110, 023002 (2013).

[53] F. Robicheaux, J. V. Hernandez, T. Topcu, and L. D. Noordam, Phys. Rev. A 70 042703 (2004).

[54] J. Hebling, Ka-Lo Yeh, M.C. Hoffmann, B. Bartal, and K. A. Nelson, JOSA B, 25, B6 (2008).

[55] H. Hirori, A. Doi, F. Blanchard, and K. Tanaka, Appl. Phys. Lett. 98, 091106 (2011).

[56] S. Li and R.R. Jones, Phys. Rev. Lett. 112, 143006 (2014).

[57] L.D. Noordam, D.I. Duncan, and T.F. Gallagher, Phys. Rev. A 45, 4734 (1992).

[58] N.E. Tielking and R.R. Jones, Phys. Rev. A 52, 1371 (1995).

[59] H. Park and T.F. Gallagher, Phys. Rev. A 86, 052510 (2012).

[60] M.L. Zimmerman, M.G. Littman, M.M. Kash, and D. Kleppner, Phys. Rev. A 20 2251 (1979).

[61] P. Hertz, Math. Ann. 67 387 (1909).

[62] B. Yan, S.A. Moses, B. Gadway, J.P. Covey, K.R.A. Hazzard, A.M. Rey, D.S. Jin, and J. Ye, Nature 501, 521 (2013).